



12-2009

Multiple Axisymmetric Solutions for Axially Traveling Waves in Solid Rocket Motors

Nadim Yaacoub Zgheib
University of Tennessee - Knoxville

Follow this and additional works at: https://trace.tennessee.edu/utk_gradthes



Part of the [Aerospace Engineering Commons](#)

Recommended Citation

Zgheib, Nadim Yaacoub, "Multiple Axisymmetric Solutions for Axially Traveling Waves in Solid Rocket Motors. " Master's Thesis, University of Tennessee, 2009.
https://trace.tennessee.edu/utk_gradthes/575

This Thesis is brought to you for free and open access by the Graduate School at TRACE: Tennessee Research and Creative Exchange. It has been accepted for inclusion in Masters Theses by an authorized administrator of TRACE: Tennessee Research and Creative Exchange. For more information, please contact trace@utk.edu.

To the Graduate Council:

I am submitting herewith a thesis written by Nadim Yaacoub Zgheib entitled "Multiple Axisymmetric Solutions for Axially Traveling Waves in Solid Rocket Motors." I have examined the final electronic copy of this thesis for form and content and recommend that it be accepted in partial fulfillment of the requirements for the degree of Master of Science, with a major in Aerospace Engineering.

Joseph Majdalani, Major Professor

We have read this thesis and recommend its acceptance:

Basil Antar, Trevor Moeller

Accepted for the Council:

Carolyn R. Hodges

Vice Provost and Dean of the Graduate School

(Original signatures are on file with official student records.)

To the Graduate Council:

I am submitting herewith a thesis written by Nadim Yaacoub Zgheib entitled “Multiple Axisymmetric Solutions for Axially Traveling Waves in Solid Rocket Motors.” I have examined the final electronic copy of this thesis for form and content and recommend that it be accepted in partial fulfillment of the requirements for the degree of Master of Science, with a major in Aerospace Engineering.

Joseph Majdalani , Major Professor

We have read this thesis
and recommend its acceptance:

Basil Antar

Trevor Moeller

Accepted for the Council:

Carolyn R. Hodges
Vice Provost and Dean of the Graduate School

(Original signatures are on file with official student records.)

Multiple Axisymmetric Solutions for Axially Traveling Waves in Solid
Rocket Motors

A Thesis Presented for
the Master of Science
Degree
The University of Tennessee, Knoxville

Nadim Yaacoub Zgheib
December 2009

Copyright © 2009 by Nadim Yaacoub Zgheib
All rights reserved.

Acknowledgement

I am grateful for my family, without their love and support I would not be where I am today. I would like to thank my advisor, Dr. Majdalani for his guidance and valuable suggestions that made this study possible. Thank you Dr. Antar and Dr. Moeller for your constructive comments that helped to improve the final work. I am thankful for the funding support of the UT Space Institute and the National Science Foundation.

Abstract

In this article, we consider the vorticoacoustic flowfield arising in a right-cylindrical porous chamber with uniform sidewall injection. Such configuration is often used to simulate the internal gaseous environment of a solid rocket motor (SRM). Assuming closed-closed acoustic conditions at both fore and aft ends of the domain, the introduction of small disturbances in the mean flow give rise to an axially traveling vortico-acoustically dominated wave structure that our study attempts to elucidate. Although this problem has been formulated before, it is reconsidered here in the context of WKB perturbation expansions in the reciprocal of the crossflow Reynolds number. This enables us to uncover multiple distinguished limits along with new asymptotic solutions that are presented for the first time. Among them are WKB approximations of type II and III that are systematically evaluated and discussed. The WKB solutions are shown to exhibit a peculiar singularity that warrants the use of matched asymptotic expansions to produce uniformly valid representations. Our solutions are obtained for any characteristic mean flow function satisfying Berman's similarity condition for porous tubes. They are also derived to an arbitrary level of precision using a recursive formulation that can reproduce each of the asymptotic solutions to any prescribed order. Finally, our solutions are verified numerically over a wide range of physical parameters and through limiting process approximations.

Table of Contents

Chapter 1	Introduction.....	1
Chapter 2	Perturbation Theory	8
2.1	Introduction	8
2.2	WKB theory	12
2.3	Matched asymptotic expansions.....	13
Chapter 3	Problem Definition.....	15
3.1	The finite channel.....	15
3.2	Mean flow solution.....	16
3.3	Linearized Navier-Stokes equations.....	18
3.4	Velocity vector decomposition.....	19
3.4.1	Irrotational response.....	20
3.4.2	Rotational response.....	20
Chapter 4	Analytical and Numerical Solutions	23
4.1	The WKB technique.....	23
4.1.1	The WKB solution of type I: $\delta = \sqrt{\varepsilon}$ and $S = O(\sqrt{R})$	24
4.1.2	The WKB solution of type II: $\delta = \varepsilon$ and $S = O(R)$	26
4.1.3	Other possible limits: $\delta = \varepsilon^{1/3}$ and $S = O(\sqrt[3]{R})$	29
4.1.4	The total velocity field.....	32
4.2	Near core approximations	35
4.2.1	WKB type I.....	36
4.2.2	WKB type II.....	37
4.3	Matched asymptotic expansions.....	39
4.3.1	Outer approximation	40

4.3.2	Inner core approximation.....	41
4.3.3	The composite solution.....	46
4.4	Special case of an exact solution.....	47
4.5	Numerical Solution	49
Chapter 5	Results and Discussion	52
Chapter 6	Conclusions and Recommendations	61
References	63
Vita	68

List of Tables

Table 2.1 Percent error at $O(\varepsilon^2)$ versus ε	11
Table 4.1. Numerical and asymptotic solutions using $S = 10$, $R = 100$, $n = 0$, and $F = r^2(2 - r^2)$	30
Table 4.2. Numerical and asymptotic solutions using $S = 50$, $R = 10000$, $n = 0$, and $F = \sin\left(\frac{1}{2}\pi r^2\right)$	31
Table 4.3. Singularity pattern for the WKB type I and type II solutions.....	38
Table 4.4. Numerical and asymptotic solutions using $S = 10$, $R = 10^3$, $n = 0$, and $F = \sin\left(\frac{1}{2}\pi r^2\right)$	46
Table 4.5. Numerical, exact, and asymptotic solutions at $O(\varepsilon)$ for $S = 20$, $R = 10^3$, $n = 0$, and $F = \frac{1}{2}\pi r^2$	49

List of Figures

Figure 3.1 Right-cylindrical tube with injecting sidewall in which vorticoacoustic oscillations are sustained..... 15

Figure 4.1. Numerical and analytical WKB type II solutions of the axially traveling wave for $F = \sin\left(\frac{1}{2}\pi r^2\right)$, $\varepsilon S^2 = 5$, $\omega_m t = \pi / 2$, $x / L = 0.5$, and a Strouhal number of a) $S = 50$ and b) $S = 100$. Fixing the penetration number $S_p = R / S^2 = 0.2$ results in a constant boundary layer thickness. 36

Figure 4.2. Residue error in the net inner correction away from the centerline. The value of the Strouhal number is kept constant as we allow the crossflow Reynolds number to vary. Four cases are considered: a) $R = 10^4$, b) 5×10^4 , c) 10^5 , and d) 10^6 . Evidently, the larger the crossflow Reynolds number, the smaller the residue. 44

Figure 4.3 Asymptotic behavior of a) E_{\max}^{ni} , and b) E_{\max}^o . Four values of the Strouhal number are considered: $S = 10, 20, 50$, and 100 45

Figure 5.1. Analytical (WKB type II) and numerical solutions of the axially traveling wave for $F = \sin\left(\frac{1}{2}\pi r^2\right)$, $S_p = 5$, $m = 1$, $\omega_m t = \pi / 2$, $x / l = 0.5$, and a Strouhal number of: a) $S = 50, 100, 200$, and 400 . With a fixed penetration number, the penetration depth y_p remains constant regardless of the wall

injection velocity or frequency of oscillations. Despite the wave's increased spatial frequency, the agreement between numerics and asymptotics seems excellent. 54

Figure 5.2 Analytical (WKB type II) and numerical solutions of the axially traveling wave for $F = \sin\left(\frac{1}{2}\pi r^2\right)$, $\varepsilon S = 0.1$, $m = 1$, $\omega_m t = \pi / 2$, $x / l = 0.5$, and a Strouhal number of: a) $S = 20, 50, 100$, and 200 . When ε and S scale according to $\varepsilon S = \text{const}$, the pattern observed is an increase in the wave intensity accompanied by a decrease in the penetration depth when the value of SR increases. Here, the analytical solution is a mirror image of its numerical counterpart. 55

Figure 5.3 a) Penetration depth y_p vs S for multiple values of R . When R is held constant, y_p decreases with higher frequencies. Also the sensitivity of y_p on S is amplified at large Strouhal numbers; b) y_p vs S for multiple values of ξ . Note that y_p remains constant when ξ is fixed and S is increased above a critical, relatively small, value. c) y_p vs S for multiple values of εS . Unlike case b, y_p diminishes as εS is increased. d) y_p vs S_p , y_p is most susceptible to change when $0.02 \leq S_p \leq 1$ 57

Figure 5.4 Penetration depth vs x for $S = 100$, $m = 1, 2, 3$ with $\xi = 0.1$ and 3 . Only the mode number is allowed to change, while ξ is kept constant. 58

Figure 5.5 WKB type II modulus of the time-dependent velocity $u_1(x, r, t)$ for the first three oscillation modes. Results are shown at equal intervals along the tube. Here $R = 10^4$ and $S = 100m$ with $m = 1, 2, 3$ 59

Chapter 1 Introduction

The study at hand involves describing the unsteady motion of a viscous fluid inside a porous tube. This problem is quite essential and vital in rocketry as it helps to simulate the behavior inside a solid rocket motor represented here by a porous cylindrical tube. As with most problems, this research line of inquiry has evolved over time. It first started with Berman (1953) who transformed the Navier-Stokes equations to a single ordinary differential equation and solved it to obtain a complete description of the fluid flow in a rectangular channel having two equally porous walls. The scope of his solution was limited to two-dimensional, incompressible, steady-state laminar flow with uniform injection or suction across the chamber's sidewalls. Several studies followed, and these focused on specific ranges of injection or suction.

For circular pipes and tubes, Yuan and Finkelstein (1956) provided, through the use of a regular perturbation technique, unique asymptotic solutions for large injection and suction as well as for the limiting case of small suction. For the case of large injection, their analytical solution applied everywhere except near the centerline, where a viscous boundary layer existed. A key parameter in their study was the crossflow Reynolds R number which was based on the uniform injection speed V , the tube radius

a , and the kinematic viscosity ν . Their solution for large R correctly reduced to the inviscid Taylor solution (Taylor, 1956) for infinite injection.

The circular tube problem was also examined by Terrill and Thomas (1969). Their numerical investigations showed that dual solutions existed for all ranges of suction and injection. For the case of large injection, they obtained two solutions, one with a viscous boundary layer at the center of the tube and one without. In an attempt to confirm their numerical solutions, they formulated analytical expressions for large injection and suction; the method of inner and outer expansions was specifically used to validate the presence of the viscous layer for large injection. The issue of the existence of multiple solutions was later examined by Skalak and Wang (1978) for the channel as well as the tube geometry. For the channel case, they showed that the solution for injection is unique, but there existed three solutions for suction. As for the cylindrical tube, they identified two types of solutions for injection and small suction, and up to four possible solutions for large suction. Thus, for circular tubes, it was concluded that there existed two solutions for injection and at most four solutions for sufficiently large suction.

So far we have only discussed the work done on steady flows in porous channels or cylinders. This problem becomes more interesting and rich with the superposition of small amplitude oscillatory waves to its steady mean flow. The modeling of oscillatory flows in injection-driven tubes or channels is pertinent to several applications. These include surface ablation, arterial blood flow modeling, and acoustic instability. The oscillatory waves under consideration may be either induced internally through intrinsic

coupling with the chamber's natural frequency, or externally, through the use of generators. The latter has been used in several cold flow experiments.

Dunlap (1990) tried to experimentally characterize the steady and oscillatory flowfields developing along the length of a simulated port rocket chamber. Their apparatus employed cylindrical porous tubes to supply uniform injection, and their experiments were conducted at injection Reynolds numbers of up to 1.2×10^4 , which is typical of rocket motor values. Flow simulation of the burning propellant was achieved by uniformly inserting ambient temperature nitrogen gas along the tube's wall. This simulation technique was primarily used in some of the first cylindrical port studies where a hot-wire anemometer was used to capture the velocity field (Dunlap et al., 1974). Multiple experiments were conducted with chamber L / D ratios of 9.5 and 14.3, where the steady and oscillatory speeds and shear stresses were evaluated in the primary coordinate directions using three element hot-wire anemometers.

In an attempt to explore the velocity coupling phenomenon observed in acoustically unstable solid rocket motors, Ma (1991) developed an inventive simulation facility in which solid carbon dioxide was used as the simulated propellant. As for the acoustic disturbances, these were introduced over the dry ice surface via a mechanically driven piston located at the end of the tube. The mean flow rate and pressure amplitude measurements revealed a coupling mechanism between the velocity component of the acoustic disturbance and the sublimation process.

Numerical studies of the flowfield over a transpiring wall in a cylindrical port were consequently carried out by Beddini and Roberts (1992) and Griffond and Casalis

(2000). Beddini's work sought to identify and quantify the role of acoustically provoked turbulence in the combustion response of solid rocket motors. As for Griffond and Casalis (2000), they explored the stability of an incompressible fluid flow inside circular cylindrical tubes with an injecting sidewall. Griffond and Casalis (2000) employed a Local Nonparallel (LNP) hydrodynamic instability approach with special treatment near the centerline. Their solution revealed a stable flowfield near the headwall and up to a critical axial position beyond which the flow became unstable. Instability occurred over a range of frequencies that widened as the distance from the headwall increased. When compared to experimental results by Dunlap (1990), their solution confirmed the existence of amplified instability waves.

Maybe one of the toughest branches of analysis of oscillatory waves in tubes and channels with transpiring walls is the analytical branch. Culick (1966) and Flandro (1974) were among the first to develop theoretical models for oscillatory flows inside porous walls. In one of his papers, Culick (1966) formulated an analytical solution for the steady, incompressible, and inviscid flowfield inside a cylindrical tube, subject to the boundary condition that the fluid was injected perpendicular to the burning propellant surface. This flow has a remarkable and distinctive feature that while satisfying the inviscid equations of motion, it also enforces the no-slip boundary condition associated with a viscous fluid. Culick's mean flow solution was indeed a good representation of the practically viscous problem as it compared favorably with the experimental results of Dunlap (1990).

Later, Flandro (1974) investigated the acoustic behavior of solid rocket propellants, where he examined the effects of the specific acoustic admittance for a burning propellant surface. Flandro employed a mathematical perturbation approach in linearizing the equations of motion for viscous, Newtonian fluids. He concluded that the propellant response to incident acoustic waves is influenced by the orientation of the propellant surface to the waves, and that the presence of a tangential component of acoustic velocity gives rise to traveling shear waves that alter the apparent propellant behavior.

Perturbation theory would later appear in several studies involving unsteady flows. Majdalani and Van Moorhem (1997) employed a Multiple Scales solution in an attempt to identify the acoustic boundary layer developing in solid rocket motors. Majdalani (1995) examined the effect of several parameters on the development and size of the boundary layer. It was concluded that the crossflow Reynolds number along with the Strouhal number dictated to a large extent the penetration depth of the wave, the region where rotational effects were present. The aforementioned dimensionless numbers were combined to form a new similarity parameter termed the penetration number, $S_p = R / S^2$, where R and S represented the crossflow Reynolds number and the Strouhal number respectively. This number was found to control the shape and size of the outer boundary layer envelope. Additionally, Majdalani (1999b) extended his work to the Cartesian domain where he tackled the two dimensional channel problem. He would once again employ Multiple Scales as the primary perturbation technique. The asymptotic solution found by Majdalani was practical in the sense that it was simple and

compact. However, it depended on the size of the perturbation parameter ε , the reciprocal of the kinetic Reynolds number. To generalize, Majdalani (2001a) formulated an exact analytical solution that is independent of ε , and thus applicable over a wider range of parameters. The study also included a leading order WKB formulation, which coincided with the leading order term of the former Multiple Scales solution. During the same year, Majdalani (2001b) used three perturbations schemes in solving for the laminar oscillatory flow in porous channels. One formulation was obtained from the vorticity transport equation, while the other two were arrived at through the use of WKB and multiple scale expansions. Despite the dissimilar expressions for the different perturbation methods, his solutions, when compared, agreed favorably with one another. However, an absolute error analysis showed that the Multiple Scale solution was the most accurate of the three.

The quest for finding the analytical technique that is most suitable for capturing the unsteady wave behavior continued. Majdalani and Flandro (2002) surveyed six perturbation solutions for the axially traveling unsteady wave in porous tubes. These were derived using (1) the composite scaling technique (Majdalani and Van Moorhem, 1997), (2) the undetermined scaling technique (Majdalani, 2001b), (3) the generalized scaling technique (Majdalani and Rienstra, 2002), (4) the WKB type I technique (Majdalani and Rienstra, 2002), (5) the vorticity transport formulation (Majdalani, 2001c; Majdalani and Roh, 2001), all of the others were based on the momentum equation, and (6) Zhao's *ad hoc* singular approach (Majdalani and Flandro, 2002). Through a

maximum absolute error analysis, it was determined that the WKB solutions outperformed other models for the large injection case.

The purpose of this study is to derive an accurate, uniformly valid asymptotic solution to the axisymmetric oscillatory field in a tube with injecting sidewalls. The work at hand constitutes a crucial extension to a previous study by Majdalani (2009). Majdalani was successful in obtaining multiple asymptotic solutions for two dimensional porous channels, whereas in our case the solution is developed for a cylindrical tube. The present configuration is more pertinent to rocketry and other applications in which axisymmetric flows are induced. Most of the work is realized through the use of the WKB and matched asymptotic expansions methods. For readers unacquainted with perturbation theory, a brief introduction is furnished in chapter 2 with special emphasis on the WKB and matched asymptotic expansions.

This thesis is arranged into six chapters. A brief introduction to perturbation theory is presented in chapter 2; this is followed in chapter 3 by the governing equations and boundary conditions. In chapter 4, we lay out the formal procedural steps leading to a multi-order WKB expansion along with a matched asymptotic approximation. These techniques are compared to a robust numerical solution. The results are later discussed in chapter 5. Finally, main conclusions are reviewed in chapter 6 along with recommendations for future analysis.

Chapter 2 Perturbation Theory

2.1 Introduction

Perturbation theory is a compilation of schemes for the systematic analysis of the global behavior of solutions to differential and difference equations. The theory first appeared in one of the oldest branches of applied mathematics: celestial mechanics, the study of the motions of the planets (Murdock, 1999). Historically, scientists would attempt to describe the motion of planets with no concrete explanation of the factors at play. Newton's formulation of the law of gravity made it possible to link planetary motion to rigorous physical laws. Theoretically, if only one planet was orbiting the sun, the motion would be elliptical with the sun at its focus. However, since there are multiple planets circling the sun and because all of these planets interact with one another, the actually observed path became a modified or perturbed elliptical motion. The way that perturbation theory works is by first assuming an unperturbed solution, usually called the leading order solution, which in our case would be to presume elliptical motion of all planets. Then, we take into account the gravitational forces exerted by the planets on each other and modify our initial guess, the unperturbed solution. After the solution is obtained, we would, once again, account for the inter-planetary forces and make the

proper corrections until our solution converges, or until the error falls within predetermined tolerance levels. Perturbation theory becomes especially valuable in cases such as these when the final solution requires few corrections to the unperturbed or leading order solution.

Nowadays, perturbation theory is being applied to a variety of fields, but the main idea behind it remains the same. The first step is to solve the simplified or unperturbed problem and then to use that solution as a first guess to the solution of the desired and more complicated problem, which generally differs from the simplified problem by a small number of terms. The second step would be to add successive corrections to the unperturbed solution until one is satisfied with the end result, when the error falls below a certain value.

To get a better grasp of the theory, the solution to one of the simpler problems will now be carried out. Finding roots of polynomials is one of the relatively straightforward problems that can be tackled by perturbation tools. The problem is purely mathematical so there would be no need to address physical issues; moreover, the problem is differentially free so that the only difficulty arises from the perturbation method itself.

Consider the following quadratic equation

$$x^2 + 2.01x - 2.98 = 0 \tag{2.1}$$

Equation (2.1) can be rewritten in terms of a “small” perturbation parameter $\varepsilon = 0.01$ as

$$x^2 + (2 + \varepsilon)x - (3 - 2\varepsilon) = 0 \tag{2.2}$$

Perturbation theory suggests expressing the solution in terms of a power series in ε

$$x = x_0 + \varepsilon x_1 + \varepsilon^2 x_2 + \dots = \sum_{i=0}^{n-1} \varepsilon^i x_i + O(\varepsilon^n) \quad (2.3)$$

The leading order solution in Eq. (2.3) is x_0 ; it represents the solution to the quadratic equation, Eq. (2.1), with a zero perturbation parameter, $\varepsilon = 0$. The solution, Eq. (2.3), may be truncated at any order, depending on the desired level of accuracy. If we were to discard all terms of order ε^3 and higher, our solution would then be exact up to $O(\varepsilon^3)$.

Replacing Eq. (2.3) back into Eq. (2.2) and collecting terms of the same order in ε up to $O(\varepsilon^2)$, we obtain

$$\begin{aligned} O(\varepsilon^0) : x_0^2 + 2x_0 - 3 &= 0 \\ O(\varepsilon^1) : x_1(2x_0 + 2) + x_0 + 2 &= 0 \\ O(\varepsilon^2) : x_2(2x_0 + 2) + x_1 + x_1^2 &= 0 \end{aligned} \quad (2.4)$$

The leading order solution x_0 is quadratic and admits two roots, let x_A and x_B represent the first and second roots, respectively. We get

$$\begin{aligned} x_A &= 1 - \frac{3}{4}\varepsilon + \frac{3}{64}\varepsilon^2 + O(\varepsilon^3) \\ x_B &= -3 - \frac{1}{4}\varepsilon - \frac{3}{64}\varepsilon^2 + O(\varepsilon^3) \end{aligned} \quad (2.5)$$

Table 2.1 shows the absolute value of the error between the exact values of the roots of Eq. (2.1) and the values obtained using a perturbation approach. The error between the exact and asymptotic values drops exponentially as our perturbation parameter is decreased. An error below 2% is achieved for a relatively large perturbation parameter of $\varepsilon = 0.5$.

Table 2.1 Percent error at $O(\varepsilon^2)$ versus ε

ε	<u>Absolute value of percent error</u>	
	x_A	x_B
0.50	1.95442	0.39709
0.10	0.05128	0.01569
0.05	0.01225	0.00391
0.01	0.00047	0.00016

In order for perturbation theory to work, the problem must have a small or large parameter, which would be used to form the power series solution. The smaller (or larger) that parameter is, the less the terms that need to be retained for an accurate compact solution. Moreover, by transforming the problem from Eq. (2.1) to Eq. (2.2), we have converted our specific problem to a more general family of problems that works with a whole range of values for the perturbation parameter; nonetheless, the accuracy of the solution remains strongly dependent on the size of ε and the order at which it is truncated.

Several theories emerged from perturbation theory, each aimed at solving specific problems with certain characteristics. These theories include: WKB technique, matched asymptotic expansions, multiple scale analysis, generalized scaling technique and others. For the study at hand, both the WKB and the matched asymptotic expansion theories will be applied. A brief introduction to these is given below.

2.2 WKB theory

The WKB technique is widely used in obtaining estimates to solutions of linear differential equations where the highest derivative is multiplied by a small, perturbation parameter. The WKB theory is well suited for describing phenomena of a dissipative or dispersive nature. Moreover, for differential equations that display such behavior, it is natural to seek a solution with an exponential nature. With this in mind, the WKB approximation of the solution to a differential equation bears the following structure

$$y(x) = \exp\left[\delta^{-1} \sum_{i=0}^{\infty} \delta^i S_i(x)\right], \quad \delta \rightarrow 0 \quad (2.6)$$

where $y(x)$ and x are the dependent and independent variables for a given differential equation having δ as the perturbation parameter. Equation (2.6) represents the initial expression from which all WKB solutions are developed. Unlike regular perturbations, the leading order term for the WKB approximation incorporates not one, but two terms, $S_0(x)$ and $S_1(x)$. The leading order solution $y^{(0)}(x)$ may be expressed as

$$y^{(0)}(x) = \exp\left[\delta^{-1} S_0(x) + S_1(x)\right] + O(\delta) \quad (2.7)$$

The equation for S_0 is termed the eikonal equation, and that for S_1 is named the transport equation. These equations as well as those for the higher order terms consist of elementary integrals of algebraic functions. In summary, the WKB technique is a powerful method for obtaining approximate solutions for suitable linear differential equations of any order. Nonetheless, its limitation lies in the fact that it cannot handle nonlinear equations.

2.3 Matched asymptotic expansions

Matched asymptotic expansions is a powerful tool for obtaining global approximations to the solution of problems involving more than one scale. A good example would be the simple flow of a viscous fluid over a flat plate. That flow has, in general, two distinguished regions, namely the viscous boundary layer and the outer section unaffected by the presence of the wall. The latter is what we call a slow varying region where a function, say velocity, changes its value by $O(1)$ over an interval of size $O(1)$. On the other hand, the viscous sublayer is a rapidly varying region in which the velocity, for example, changes its value quickly by $O(1)$ over an interval whose size is ever small approaching 0. The matched asymptotic expansions technique splits the domain into several parts depending on the number of scales exhibited by the problem. By identifying one region for every scale, it then rescales the variables in their corresponding domains. Each region would thus be solved for separately, and eventually, the solutions would be matched to arrive at the final matched asymptotic expansions solution.

The problems we confront in fluid mechanics as well as other disciplines comprise mostly nonlinear governing equations as well as nonlinear boundary conditions. Accordingly, numerical and analytical techniques are used separately or mutually, when possible, to obtain approximate or at times exact solutions. If one is to acquire some insight into the behavior of the solution of nonlinear problems and their dependence on certain parameters, it might be necessary to repeat the calculations for different values of those parameters. In contrast, analytical methods can often delineate general phenomena

leading to closed form approximations. In the case of nonlinear partial differential equations with variable coefficients, the combination of both analytical and numerical methods may offer the best avenue for analysis. When the problem exhibits a condition where one or more parameters are either very small or very large, a straightforward numerical procedure becomes difficult to obtain. In this situation, analytical methods offer a reliable alternative that is less costly and more universal.

Chapter 3 Problem Definition

3.1 The finite channel

The flow under consideration is established inside a long porous cylindrical tube of radius a and length L ; a schematic of the geometry is depicted in Figure 3.1. A Newtonian fluid is injected with a uniform speed V through the tube's sidewall. Throughout this study, we will in fact, limit our attention to a perfect gas. The spatial dimensional variables x^* and r^* will be normalized by the tube's radius a . Taking the tube's axial symmetry into account, the scope of our study is reduced to $0 \leq x \leq l$ and

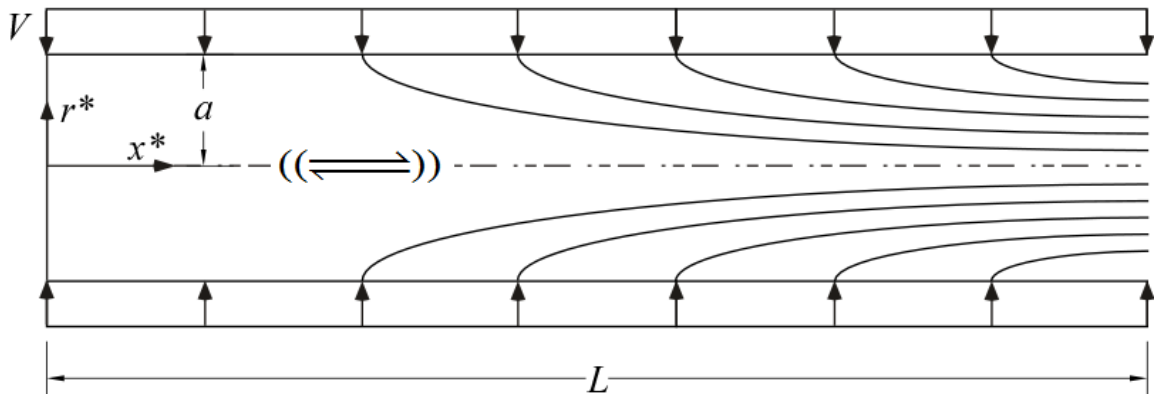


Figure 3.1 Right-cylindrical tube with injecting sidewall in which vorticoacoustic oscillations are sustained.

$0 \leq r \leq 1$, where x and r represent, in that order, the tube's non-dimensional axial and radial coordinates, and l denotes the tube's non-dimensional length $l = L / a < 70$. With the tube being closed at the head end (zero inlet profile in Berman's formulation) and choked at the downstream end, small fluctuations in the injection velocity give rise to a harmonic oscillatory pressure field of frequency ω and amplitude A . It is this oscillatory field that we wish to analyze. Following Majdalani and Roh (2000), we consider low crossflow Mach numbers ($M = V / c < 0.01$), c being the speed of sound, and small pressure amplitudes A relative to the mean stagnation pressure p_s .

3.2 Mean flow solution

Our point of departure is the self-similar mean-flow solution in a circular cylinder with porous walls. According to Berman (1953), if we allow the stream function Ψ to vary linearly with the cylinder's longitudinal axis (x -axis), $\Psi = xF(r)$ (Weissberg, 1959; Brady and Acrivos, 1981), the Navier-Stokes equations reduce to a linear fourth order ordinary differential equation with variable coefficients. We recover:

$$r^3 F^{(4)} + r^2 R F^{(3)}(F - 2\varepsilon) + R(F' - rF'')[rF' + 3(F - \varepsilon)] = 0; \quad \varepsilon \equiv 1 / R \quad (3.1)$$

with R being the injection crossflow Reynolds number $R = Va / \nu$. The mean flow velocity and vorticity vectors are normalized by V and defined as $\mathbf{u}_0 = u_0 \mathbf{e}_x + v_0 \mathbf{e}_r$ and $\mathbf{\Omega}_0 = \Omega_0 \mathbf{e}_\theta$. Equation (3.1) requires four boundary conditions: (1) the no slip boundary $u_0(x,1) = 0$, (2) axial symmetry $\partial u_0(x,0) / \partial r = 0$, (3) radial influx at the wall

$v_0(x,1) = -1$, and (4) boundedness at the centerline $v_0(x,0) = 0$. Recalling the definition for the stream function in cylindrical coordinates, one may write

$$u_0 = \frac{1}{r} \frac{\partial \Psi}{\partial r} = \frac{x F'}{r}; \quad v_0 = -\frac{1}{r} \frac{\partial \Psi}{\partial x} = -\frac{F}{r}; \quad \Omega_0 = \frac{x(F' / r - F'')}{r} \quad (3.2)$$

Inserting the boundary conditions into Eq. (3.2), we obtain

$$F(1) = 1; \quad F'(1) = F(0) = 0; \quad \lim_{r \rightarrow 0} \frac{F'' - F' / r}{r} = 0 \quad (3.3)$$

Depending on the size of the crossflow Reynolds number, different values for F are available (Terrill, 1983). However, for a tube experiencing either large or small sidewall injection, Yuan and Finkelstein (1956) suggest two solutions for F , specifically

$$F(r) = \begin{cases} r^2(2 - r^2) + O(10^{-2} R r^2); & 10 < R < 100 \\ \sin(\frac{1}{2} \pi r^2) + O(R^{-1}); & R > 100 \end{cases} \quad (3.4)$$

Replacing Eq. (3.4) back into Eq. (3.2) and ignoring terms of higher order, one can write

$$\begin{cases} u_0 = 4x(1 - r^2); & v_0 = r^3 - 2r; & \Omega_0 = 8rx; & 10 < R < 100 \\ u_0 = \pi x \cos(\frac{1}{2} \pi r^2); & v_0 = -\frac{1}{r} \sin(\frac{1}{2} \pi r^2); & \Omega_0 = \pi^2 r x \sin(\frac{1}{2} \pi r^2); & R > 100 \end{cases} \quad (3.5)$$

Following Majdalani and Flandro (2002), the mean pressure associated with Eq. (3.2) is normalized by γp_s , with γ being the ratio of specific heats, and integrated from the steady flow momentum equation, $\mathbf{u}_0 \cdot \nabla \mathbf{u}_0 = -M^{-2} \nabla p_0 + \varepsilon \nabla^2 \mathbf{u}_0$. Keeping in mind that $c = \sqrt{\gamma p_s / \rho_s}$ and that $p_0(0,0) = 1 / \gamma$, we get

$$\begin{cases} p_0 = \frac{1}{\gamma} - \frac{1}{2} r^{-2} M^2 \{F^2 + x^2 [F'^2 + (r^{-1} F' - F'')(F - \varepsilon) - \varepsilon r F'''] + \varepsilon r F'\} \\ = \gamma^{-1} + O(M^2 x^2) \end{cases} \quad (3.6)$$

Equation (3.6) shows that the pressure is almost constant along the tube with low dependency on axial location.

3.3 Linearized Navier-Stokes equations

In normalizing variables, we shall use the asterisks to denote dimensional quantities. The spatial coordinates, pressure, velocity, density, and time are normalized as

$$x = \frac{x^*}{a}; \quad r = \frac{r^*}{a}; \quad p = \frac{p^*}{\gamma p_s}; \quad \mathbf{u} = \frac{\mathbf{u}^*}{c}; \quad \rho = \frac{\rho^*}{\rho_s}; \quad t = \frac{t^*}{a/c} \quad (3.7)$$

Working with these non-dimensional quantities, and assuming constant kinematic viscosity and negligible bulk viscosity, the mass and momentum conservation equations become

$$\frac{\partial \rho}{\partial t} + \nabla \cdot (\rho \mathbf{u}) = 0 \quad (3.8)$$

$$\rho \left[\frac{\partial \mathbf{u}}{\partial t} + (\mathbf{u} \cdot \nabla) \mathbf{u} \right] = -\nabla p + \varepsilon M \left[\frac{4}{3} \nabla (\nabla \cdot \mathbf{u}) - \nabla \times (\nabla \times \mathbf{u}) \right] \quad (3.9)$$

With the inclusion of periodic fluctuations, an oscillatory time-dependent quantity must be added to the steady state component of each variable of interest, specifically

$$p = \gamma^{-1} + \bar{\varepsilon} p_1; \quad \rho = 1 + \bar{\varepsilon} \rho_1; \quad \mathbf{u} = M \mathbf{u}_0 + \bar{\varepsilon} \mathbf{u}_1; \quad \boldsymbol{\Omega}_0 = M \boldsymbol{\Omega}_0 + \bar{\varepsilon} \boldsymbol{\Omega}_1 \quad (3.10)$$

where $\bar{\varepsilon} = A / (\gamma p_s)$ is the wave amplitude ratio. If we insert Eq. (3.10) into the conservation equations, Eqs. (3.8) and (3.9), we obtain two sets of equations, namely the leading order equations, which by themselves describe the steady state problem, and the first order equations responsible for the oscillatory field inside the tube. The steady state

equations have been previously expressed for both small and large injection in Eq. (3.5).

For the first order set, we get

$$\frac{\partial \rho_1}{\partial t} + \nabla \cdot (\mathbf{u}_1) = -M \nabla \cdot (\rho_1 \mathbf{u}_0) + O(\bar{\varepsilon}) \quad (3.11)$$

$$\left\{ \begin{aligned} \frac{\partial \mathbf{u}_1}{\partial t} &= -M \left[\nabla(\mathbf{u}_0 \cdot \mathbf{u}_1) - \mathbf{u}_1 \times \boldsymbol{\Omega}_0 - \mathbf{u}_0 \times \boldsymbol{\Omega}_1 \right] \\ &\quad - \nabla p_1 + \varepsilon M \left[\frac{4}{3} \nabla(\nabla \cdot \mathbf{u}_1) - \nabla \times \boldsymbol{\Omega}_1 \right] + O(\bar{\varepsilon}) \end{aligned} \right. \quad (3.12)$$

3.4 Velocity vector decomposition

The temporal fluctuations are separated into a rotational, solenoidal response and an irrotational component. Using the circumflex and the tilde to represent the irrotational and solenoidal components, one may write

$$\mathbf{u}_1 = \hat{\mathbf{u}} + \tilde{\mathbf{u}}; \quad \boldsymbol{\Omega}_1 = \tilde{\boldsymbol{\Omega}}; \quad p_1 = \hat{p}; \quad \rho_1 = \hat{\rho} \quad (3.13)$$

Substituting Eq. (3.13) into the linearized governing equations, Eqs. (3.11) and (3.12), we obtain two distinct sets. The first is the oscillatory vortical response. It may be expressed at $O(\bar{\varepsilon})$ as

$$\nabla \cdot \tilde{\mathbf{u}} = 0; \quad \frac{\partial \tilde{\mathbf{u}}}{\partial t} = -M \left[\nabla(\tilde{\mathbf{u}} \cdot \mathbf{u}_0) - \tilde{\mathbf{u}} \times \boldsymbol{\Omega}_0 - \mathbf{u}_0 \times \tilde{\boldsymbol{\Omega}} \right] - \varepsilon M \nabla \times \tilde{\boldsymbol{\Omega}} \quad (3.14)$$

The second is the irrotational pressure driven response, again at order $O(\bar{\varepsilon})$:

$$\frac{\partial^2 \hat{p}}{\partial t^2} - \nabla^2 \hat{p} = -M \left[\nabla \cdot \left(\mathbf{u}_0 \frac{\partial \hat{p}}{\partial t} \right) - \nabla^2(\hat{\mathbf{u}} \cdot \mathbf{u}_0) + \nabla \cdot (\hat{\mathbf{u}} \times \boldsymbol{\Omega}_0) \right] - \frac{4}{3} \varepsilon M \nabla^2(\nabla \cdot \hat{\mathbf{u}}) \quad (3.15)$$

3.4.1 Irrotational response

The last term in Eq. (3.15), represents damping due to viscosity, a quantity that is of order $O(\varepsilon M)$ where $\varepsilon M < M, \forall \varepsilon < 1$. Then, if we ignore terms of $O(M)$ and smaller in Eq. (3.15), the oscillatory pressure at $O(M)$ reduces to

$$\hat{p}(x, t) = \cos(\omega_m x) \exp(-i\omega_m t) \quad (3.16)$$

where Euler's notation is used. The irrotational component at $O(M)$ of the velocity is readily obtained by substituting Eq. (3.16) into Eq. (3.12) and ignoring higher order terms

$$\hat{u}(x, t) = i \sin(\omega_m x) \exp(-i\omega_m t) \quad (3.17)$$

where ω_m denotes the oscillation mode number for a cylindrical tube that is acoustically closed at both ends.

$$\omega_m = \omega a / c = m\pi / l, m \in \mathbb{N}^* \quad (3.18)$$

3.4.2 Rotational response

In a similar fashion, the oscillatory vortical response can be expressed as

$$\tilde{\mathbf{u}}(x, r, t) = \bar{\mathbf{u}}(x, r) \exp(-i\omega_m t); \quad \tilde{\boldsymbol{\Omega}}(x, r, t) = \bar{\boldsymbol{\Omega}}(x, r) \exp(-i\omega_m t) \quad (3.19)$$

with $\bar{\mathbf{u}} \equiv \bar{u}e_x + \bar{v}e_r$ and $\bar{\boldsymbol{\Omega}} \equiv \nabla \times \bar{\mathbf{u}} = \bar{\Omega}e_\theta$. In place of Eq. (3.14), we now write

$$\nabla \cdot \bar{\mathbf{u}} = O(\bar{\varepsilon}); \quad iS\bar{\mathbf{u}} = \left[\nabla(\bar{\mathbf{u}} \cdot \mathbf{u}_0) - \bar{\mathbf{u}} \times \boldsymbol{\Omega}_0 - \mathbf{u}_0 \times \bar{\boldsymbol{\Omega}} \right] + \varepsilon \nabla \times \bar{\boldsymbol{\Omega}} + O(\bar{\varepsilon}M^{-1}) \quad (3.20)$$

with $S = \omega a / V$ being the Strouhal number.

In determining the relative sizes of $\bar{\varepsilon}$ and M , we adopt an ordering scheme used in combustion stability theory. We thus put

$$M^2 < \bar{\varepsilon} < M; \quad \lim_{\bar{\varepsilon}, M \rightarrow 0} \frac{\bar{\varepsilon}}{M} = 0 \quad (3.21)$$

If we then follow Majdalani and Roh (2000) by taking $\bar{v} / \bar{u} = O(M)$, the axial component of the velocity in Eq. (3.20) may be expressed as

$$iS\bar{u} = \frac{\partial(u_0\bar{u})}{\partial x} + v_0 \frac{\partial\bar{u}}{\partial r} - \varepsilon \frac{1}{r} \frac{\partial}{\partial r} \left(r \frac{\partial\bar{u}}{\partial r} \right) \quad (3.22)$$

To obtain \bar{u} from Eq. (3.22), the latter must first be rearranged into

$$x \frac{\partial\bar{u}}{\partial x} = \left(\frac{irS}{F'} - 1 \right) \bar{u} + \frac{F}{F'} \frac{\partial\bar{u}}{\partial r} + \varepsilon \frac{r}{F'} \left(\frac{\partial^2\bar{u}}{\partial r^2} + \frac{1}{r} \frac{\partial\bar{u}}{\partial r} \right) \quad (3.23)$$

At this point, we may use the separated variable form, $\bar{u}(x, r) = X(x)R(r)$, in Eq. (3.23). Then as shown by Majdalani and Flandro (2002), we may enforce the no slip condition at the sidewall, $\bar{u}(x, 1) + i \sin(\omega_m x) = 0$, to obtain

$$\bar{u}(x, r) = -i \sum_{n=0}^{\infty} (-1)^n \frac{(\omega_m x)^{2n+1}}{(2n+1)!} R_n(r) \quad (3.24)$$

where the eigenfunction $R_n(r)$ is determined from

$$\begin{aligned} \varepsilon \frac{d^2 R_n}{dr^2} + \frac{(\varepsilon + F)}{r} \frac{dR_n}{dr} + \left[iS - 2(n+1) \frac{F'}{r} \right] R_n &= 0; \quad 0 \leq r \leq 1; \\ R_n(1) &= 1; \quad R'_n(0) = 0 \end{aligned} \quad (3.25)$$

where $R_n(1) = 1$ and $R'_n(0) = 0$ represent the no-slip and symmetry boundary conditions respectively.

The total axial velocity can now be retrieved by summing up its irrotational and solenoidal counterparts; one collects

$$u_1(x, r, t) = \sin(\omega_m x) \sin(\omega_m t) - i \sum_{n=0}^{\infty} (-1)^n \frac{(\omega_m x)^{2n+1}}{(2n+1)!} R_n(r) \exp(-i\omega_m t) \quad (3.26)$$

In what follows, several analytical methods will be used to solve Eq. (3.25) and overcome its inherent singularity at the core. These will be confirmed numerically.

Chapter 4 Analytical and Numerical Solutions

4.1 The WKB technique

Closed form representations of Eq. (3.25) are intractable due to the general coefficients in the second and third terms. The inherently stiff nature of the problem also renders numerical solutions difficult to obtain for large Reynolds numbers. In contrast, highly accurate asymptotic approximations can be arrived at using the Wentzel-Kramers-Brillouin expansion method or WKB for short. Generally, the WKB technique is often employed in solving linear differential equations exhibiting oscillatory behavior, in which the highest derivative is multiplied by a small parameter. Formal WKB theory (Bender and Orszag, 1978) suggests setting

$$R_n(r) = \exp(\delta^{-1}S_0 + S_1 + \delta S_2 + \delta^2 S_3 + \delta^3 S_4 + \dots) \quad (4.1)$$

where δ is a small parameter and $S_j(r)$ must be determined sequentially for $j \geq 0$.

Straightforward differentiation and substitution into Eq. (3.25) yields

$$\left\{ \begin{aligned} &\varepsilon \left[\delta^{-1} S_0'' + S_1'' + \delta S_2'' + \delta^{-2} S_0'^2 + S_1'^2 + 2\delta^{-1} S_0' S_1' + 2S_0' S_2' + 2\delta S_1' S_2' \right] \\ &+ \frac{1}{r} (F + \varepsilon) (\delta^{-1} S_0' + S_1' + \delta S_2') + \left[iS - 2(n+1) \frac{1}{r} F' \right] = 0 \end{aligned} \right. \quad (4.2)$$

Depending on the relative sizes of ε and δ , Eq. (4.2) gives rise to two distinguished limits, namely $\delta = \sqrt{\varepsilon}$ and $\delta = \varepsilon$.

4.1.1 The WKB solution of type I: $\delta = \sqrt{\varepsilon}$ and $S = O(\sqrt{R})$

Starting with Eq. (4.2) and replacing δ by $\sqrt{\varepsilon}$, we are left with

$$\left\{ \begin{aligned} & \frac{1}{\sqrt{\varepsilon}} \left(\frac{F}{r} S'_0 + iS\sqrt{\varepsilon} \right) + \left(S_0'^2 + \frac{F}{r} S'_1 - 2(n+1) \frac{1}{r} F' \right) \\ & + \sqrt{\varepsilon} \left(S_0'' + \frac{S'_0}{r} + 2S'_0 S'_1 + \frac{F S'_2}{r} \right) + \dots = 0 \end{aligned} \right. \quad (4.3)$$

where the quantities outside the parentheses dictate the order of the term that they multiply. In order to satisfy Eq. (4.3), quantities at every order must vanish. Therefore at $O(\varepsilon^{-1/2})$, the leading order equation is immediately realized in the form of a first order linear differential equation

$$S'_0(r) = -\frac{riS\sqrt{\varepsilon}}{F(r)}; \quad S_0(1) = 0 \quad (4.4)$$

It should be borne in mind that Eq. (4.4) does not constitute an Eikonal equation in the strict sense of the term. Typical Eikonal equations comprise a first derivative that is squared, thus leading to dual solutions. Here, only one solution is precipitated by the type I distinguished limit. As we turn our attention to the so-called transport equation, the same departure from classic behavior is realized. In fact, the higher order corrective functions, S_1 and S_2 become single valued and expressible by

$$S_1'(r) = -\frac{rS_0'^2(r) - 2(n+1)F'(r)}{F(r)}; \quad S_1(1) = 0 \quad (4.5)$$

$$S_2'(r) = -\frac{rS_0''(r)_0 + 2rS_0'(r)S_1'(r) + S_0'(r)}{F(r)}; \quad S_2(1) = 0 \quad (4.6)$$

After carrying the solution to much higher orders, a simple recursive relation is obtained, namely,

$$S_{k+2}'(r) = -\frac{1}{F} \left(S_k' + rS_k'' + r \sum_{i=0}^{k+1} S_i' S_{k+1-i}' \right), \quad S_{k+2}(1) = 0; \quad k \in \mathbb{N} \quad (4.7)$$

The type I solution may be constructed by integrating Eqs. (4.4), (4.5), and (4.6).

Carrying out the integration, one obtains,

$$S_0(r) = -iS\sqrt{\varepsilon} \int_1^r \frac{x}{F(x)} dx \quad (4.8)$$

$$S_1(r) = \xi \int_1^r \frac{x^3}{F^3(x)} dx + \ln \left[\frac{F(r)}{F(1)} \right]^{2n+2}; \quad \xi = \varepsilon S^2 \quad (4.9)$$

$$S_2(r) = iS\sqrt{\varepsilon} \left\{ \begin{aligned} & (2n + \frac{3}{2}) \left[1 - r^2 F^{-2}(r) \right] \\ & + (4n + 5) \int_1^r \left[x / F^2(x) \right] dx + 2\xi \int_1^r \left[x^5 / F^5(x) \right] dx \end{aligned} \right\} \quad (4.10)$$

Note that $\xi = \varepsilon S^2$ was first discovered by Majdalani (1995) and shown to control the amplitude of a decaying rotational wave. By substituting Eqs. (4.8), (4.9), and (4.10) back into Eq. (4.1), while realizing from Eq. (3.4) that $F(1) = 1$, one obtains the leading order type I WKB solution

$$R_n^I(r) = F^{2n+2} \exp(\zeta_0 - i\Phi_0 - i\Phi_1^n) + O(\varepsilon) \quad (4.11)$$

with

$$\left\{ \begin{array}{l} \zeta_0 = \xi \int_1^r \frac{x^3}{F^3(x)} dx; \quad \xi = \varepsilon S^2; \quad \Phi_0 = S \int_1^r \frac{x}{F(x)} dx; \\ \Phi_1^n = -\varepsilon S \left\{ \begin{array}{l} (2n + \frac{3}{2}) [1 - r^2 F^{-2}(r)] \\ + (4n + 5) \int_1^r [x / F^2(x)] dx + 2\xi \int_1^r [x^5 / F^5(x)] dx \end{array} \right\} \end{array} \right\} \quad (4.12)$$

4.1.2 The WKB solution of type II: $\delta = \varepsilon$ and $S = O(R)$

Again, we start with Eq. (4.2) and replace δ by ε then collect terms at different orders. We get

$$\left\{ \begin{array}{l} \frac{1}{\varepsilon} \left(S_0'^2 + \frac{F}{r} S_0' + i\varepsilon S \right) + \left[S_0'' + 2S_0' S_1' + \frac{1}{r} S_0' + \frac{F}{r} S_1' - 2(n+1) \frac{1}{r} F' \right] \\ + \varepsilon \left(S_1'' + S_1'^2 + 2S_0' S_2' + \frac{S_1'}{r} + \frac{F S_2'}{r} \right) + \dots = 0 \end{array} \right\} \quad (4.13)$$

The quantities inside the parentheses must sequentially vanish, starting with the lowest order. Resolution of the ε multipliers may hence be continued until a desired order is reached. For the type II case, a conventional Eikonal equation is returned, namely,

$$S_0'^2 + \frac{F}{r} S_0' + i\varepsilon S = 0 \quad (4.14)$$

Its dual roots are given by

$$\left\{ \begin{array}{l} S_{01} = -\int_1^r \frac{1}{2x} \left[F(x) + \sqrt{F(x)^2 - 4iS\varepsilon x^2} \right] dx \\ S_{02} = -\int_1^r \frac{1}{2x} \left[F(x) - \sqrt{F(x)^2 - 4iS\varepsilon x^2} \right] dx \end{array} \right\} \quad (4.15)$$

Due to the quadratic nature of the Eikonal equation and the duality of its roots, S_{01} and S_{02} , two conjugate solutions will be obtained for each of the higher order corrections S_1 , S_2 , S_3 and so on. Each of these will correspond to either S_{01} or S_{02} .

At $O(1)$, the transport equation may be solved for S_1 with the outcome,

$$S_1 = -\int_1^r \frac{xS_0''(x) + S_0'(x) - 2(n+1)F'(x)}{2xS_0'(x) + F(x)} dx \quad (4.16)$$

At $O(\varepsilon)$, S_2 begets

$$S_2 = -\int_1^r \frac{xS_1'(x) + xS_1'^2(x) + S_1'(x)}{2xS_0'(x) + F(x)} dx \quad (4.17)$$

Higher orders may be similarly achieved. After some effort, a recursive relation is developed to help reproduce the successive corrections for $k \in \mathbb{N}^*$. We have

$$S_{k+3} = -\int_1^r (F + 2rS_0')^{-1} \left(S_{k+2}' + xS_{k+2}'' + 2xS_1'S_{k+2}' + x \sum_{i=1}^k S_{i+1}' S_{k+2-i}' \right) dx \quad (4.18)$$

This recursive formula is valid for any order. In most practical applications, however, no more than three terms are needed to accurately describe the wave behavior. By substituting Eqs. (4.15), (4.16), and (4.17) into Eq. (4.1), the type II solution R_n^{II} may be arrived at. The linearity of Eq. (3.25) warrants the inclusion of both conjugates in Eq. (4.15) and higher order terms. We hence retrieve,

$$R_n^{II} = C_1 \exp(\delta^{-1}S_{01} + S_{11} + \delta S_{21}) + C_2 \exp(\delta^{-1}S_{02} + S_{12} + \delta S_{22}) \quad (4.19)$$

$$\begin{cases} S_{11} = -\int_1^r \frac{xS_{01}''(x) + S_{01}'(x) - 2(n+1)F'(x)}{2xS_{01}'(x) + F(x)} dx \\ S_{12} = -\int_1^r \frac{xS_{02}''(x) + S_{02}'(x) - 2(n+1)F'(x)}{2xS_{02}'(x) + F(x)} dx \end{cases} \quad (4.20)$$

$$\begin{cases} S_{21} = -\int_1^r \frac{xS_{11}''(x) + xS_{11}'^2(x) + S_{11}'(x)}{2xS_{01}'(x) + F(x)} dx \\ S_{22} = -\int_1^r \frac{xS_{12}''(x) + xS_{12}'^2(x) + S_{12}'(x)}{2xS_{02}'(x) + F(x)} dx \end{cases} \quad (4.21)$$

At this juncture, the problem's boundary conditions must be applied to determine the constants of integration. By taking $C_1 = 0$ and $C_2 = 1$, the boundary conditions in Eq. (3.25) may be secured while ensuring boundedness throughout the domain. The type II approximation reduces to

$$R_n^{II}(r) = \exp(\delta^{-1}S_{02} + S_{12} + \delta S_{22}) + \mathcal{O}(\delta^2) \quad (4.22)$$

For the WKB type I solution, in both the rectangular channel and the cylindrical tube, the value of R_n^I at the core alternates between zero and infinity, depending on the order at which the solution is truncated. The solution suddenly becomes unbounded at even orders in ε , $R_n^I \rightarrow \infty$ as $r \rightarrow 0$; however, for odd orders in ε , the solution is well behaved, $R_n^I \rightarrow 0$ as $r \rightarrow 0$. In reality, the numerical solution suggests that neither outcome is correct, rather the function R_n possesses an asymptotically small value at $r = 0$ that may be explicitly estimated. As for the type II solution, the cylindrical case exhibits a singular behavior at the centerline with a pattern that again alternates between zero and infinity every four orders in ε . This pattern will be discussed in detail in section

4.2.2. Contrary to the cylindrical case, the type II channel solution remains uniformly valid and singularity free throughout the entire domain.

Moreover, the type II solution for the cylindrical configuration leads to a generally quasi-analytical form that precludes the explicit integration of Eqs. (4.15), (4.16), and (4.17). For $F(r) = \sin\left(\frac{1}{2}\pi r^2\right)$, these have to be integrated numerically. This is atypical of the WKB type I formulation which has led to a fully analytical solution for this study as well as for the porous channel flow analog (Majdalani, 2009).

4.1.3 Other possible limits: $\delta = \varepsilon^{1/3}$ and $S = O\left(\sqrt[3]{R}\right)$

A type III expansion is possible granted $\delta = \varepsilon^{1/3}$. Following the same procedure as before, the leading order equation returns a first order ODE

$$S'_0 = -\frac{iS\varepsilon^{1/3}r}{F} \quad (4.23)$$

Higher orders are obtained sequentially at fractional increments of $O(\varepsilon^{1/3})$; these give

$$S'_1 = 2(n+1)F'/F \quad (4.24)$$

$$S'_2 = -rS_0'^2 / F \quad (4.25)$$

A recurrence formula is identified for $k \geq 0$, namely

$$S'_{k+3} = -\frac{1}{F} \left(S'_k + rS_k'' + r \sum_{i=0}^{k+1} S'_i S'_{k+1-i} \right); \quad k \in \mathbb{N} \quad (4.26)$$

If we compare Eq. (4.26) to the recurrence formula for the type I solution in Eq. (4.7), we find that, beyond S_3 , the type III solution begins to replicate the type I

Table 4.1. Numerical and asymptotic solutions using $S = 10$, $R = 100$, $n = 0$, and $F = r^2(2 - r^2)$

r	WKB I			WKB II			Numerical
	$O(\varepsilon)$	$O(\varepsilon^2)$	$O(\varepsilon^3)$	$O(\varepsilon)$	$O(\varepsilon^2)$	$O(\varepsilon^3)$	
0.00	0	∞	0	∞	∞	∞	-0.000095
0.05	0	∞	0	-0.000232	-0.000189	-0.000245	-0.000248
0.10	0	∞	0	-0.000464	-0.000681	-0.000794	-0.000756
0.15	-0.000077	-351.5493	0	-0.000407	-0.001307	-0.001312	-0.001261
0.20	0.000793	0.081356	-0.000001	0.001258	-0.000258	0.000071	0.000050
0.25	0.003737	-0.010881	0.001476	0.006808	0.005950	0.006450	0.006354
...							
0.75	-0.314489	-0.324418	-0.323904	-0.329651	-0.322887	-0.323929	-0.323878
0.80	-0.132432	-0.136933	-0.136969	-0.140714	-0.136146	-0.136945	-0.136903
0.85	0.163223	0.162151	0.161967	0.162109	0.162368	0.161980	0.162009
0.90	0.517807	0.517666	0.517644	0.521459	0.517614	0.517611	0.517631
0.95	0.835726	0.835242	0.835397	0.839798	0.835182	0.835339	0.835352
1.00	1.000000	1.000000	1.000000	1.000000	1.000000	1.000000	1.000000

approximation, albeit at a previous order. That is, S_3 , S_4 , and S_5 for type III reproduce S_2 , S_3 , and S_4 for type I. Therefore, for $j \geq 3$, one may write $S_j^{III} = S_{j-1}^I$. For this reason, only the type I expansion will be considered in the remainder of this study.

Furthermore, through a dual parametric trade analysis, we find the type II solution, as presented in Tables 4.1 and 4.2, to remain valid over a wide range of the Strouhal number S and the crossflow Reynolds number R . Moreover, R_n^{II} matches the numerical solution quite persistently for the different values of F , especially those obtained for medium and large injection. In contrast to the small injection case, the type I solution, as depicted in Table 4.2, shows better agreement with numerical data over a wider portion of the domain, albeit unable to capture the small oscillations about the

Table 4.2. Numerical and asymptotic solutions using $S = 50$, $R = 10000$, $n = 0$, and

$$F = \sin\left(\frac{1}{2}\pi r^2\right)$$

r	WKB I			WKB II			Numerical
	$O(\varepsilon)$	$O(\varepsilon^2)$	$O(\varepsilon^3)$	$O(\varepsilon)$	$O(\varepsilon^2)$	$O(\varepsilon^3)$	
0.00	0	∞	0	∞	∞	∞	-8.8×10^{-17}
0.05	0	-0.002275	0	2.6×10^{-9}	3.6×10^{-9}	3.6×10^{-9}	3.6×10^{-9}
0.10	0.000009	0.000014	0.000012	0.000013	0.000013	0.000013	0.000013
0.15	0.000178	0.000189	0.000189	0.000186	0.000189	0.000189	0.000189
0.20	-0.000250	-0.000251	-0.000252	-0.000252	-0.000252	-0.000252	-0.000252
0.25	-0.004322	-0.004376	-0.004376	-0.004350	-0.004376	-0.004376	-0.004377
...
0.75	0.448374	0.448333	0.448333	0.448414	0.448333	0.448333	0.448128
0.80	-0.679822	-0.679732	-0.679732	-0.679866	-0.679732	-0.679732	-0.679706
0.85	0.505482	0.505412	0.505412	0.505504	0.505412	0.505412	0.505667
0.90	0.096224	0.096212	0.096212	0.096228	0.096211	0.096212	0.095773
0.95	-0.741260	-0.741205	-0.741205	-0.741270	-0.741205	-0.741205	-0.740844
1.00	1.000000	1.000000	1.000000	1.000000	1.000000	1.000000	0.999917

centerline. Nonetheless, these oscillations are so small that they fall within the truncation error at the first order, thus making the type I solution a uniformly valid representation at that order. This cannot be said for the higher order solutions where the discrepancy around the centerline becomes larger than the truncation error itself. Under these conditions, one must insist on an inner correction, and such a correction might become useful only in applications demanding high accuracy in the core region.

In Tables 4.1 and 4.2, we inspect the accuracy of both WKB approximations by comparing them to a highly accurate numerical solution. We consider asymptotic solutions at three orders in ε , namely $\varepsilon = 1, 2$, and 3 . The alternating pattern discussed earlier in section 4.1.2 is readily observed. When $r \rightarrow 0$, $R_n^I \rightarrow 0$ at odd orders in ε , and $R_n^I \rightarrow \infty$ at even orders. As for the type II, $R_n^{II} \rightarrow \infty$ for all three truncation orders

as $r \rightarrow 0$. In Table 4.1 we use relatively small values for the Strouhal and Reynolds numbers, viz $S = 10$ and $R = 100$. At these values, Yuan and Finkelstein (1956) suggest a polynomial representation for the base solution, $F = r^2(2 - r^2)$. The singularity pattern observed in Table 4.1 remains identical to that in Table 4.2 even with the use of a different base solution, $F = \sin\left(\frac{1}{2}\pi r^2\right)$, that is appropriate for relatively large Strouhal and Reynolds numbers.

Examining Tables 4.1 and 4.2, we note an alternating pattern of singularity associated with the type I solution near $r = 0$ that changes from zero to infinity with each successive order. On the other hand, it seems that the type II solution remains singular as $r \rightarrow 0$, irrespective of the order at which the solution is truncated.

In reality, we find that the type II solution is not always singular at the core. To capture its uniformly valid behavior, at least 5 terms are needed, namely S_0, S_1, S_2, S_3 , and S_4 . In this vein, a detailed near core analysis will be required.

4.1.4 The total velocity field

The total axial velocity field is obtained by replacing the type I eigenfunction solution, Eq. (4.11), back into Eq. (3.26), and recalling that the Taylor series expansion of

the sine function about $x = \beta$ is $\sin(x - \beta) = \sum_{n=0}^{\infty} (-1)^n \frac{(x - \beta)^{2n+1}}{(2n + 1)!}$. At the outset, one

can put

$$u_1(x, r, t) = i \exp(-i\omega_m t) \left[\sin(\omega_m x) - F \sin(\omega_m x F) \exp\left(\zeta_0 - i\Phi_0 - i\Phi_1^n\right) \right] \quad (4.27)$$

Equation (4.27) comprises both a compressible and an incompressible disturbance. As such, before seeking its radial component, we will first proceed to split u_1 into \hat{u} and \tilde{u} , the irrotational compressible and the rotational incompressible components, respectively. Then from \tilde{u} , the radial component of the velocity \tilde{v} may be formulated through the following ansatz, namely,

$$\tilde{v} = ir^{-1} \exp(-i\omega_m t) G(r) \cos(\omega_m xF) \exp(\zeta_0 - i\Phi_0 - i\Phi_1^n) \quad (4.28)$$

where $G(r)$ must be determined by satisfying the continuity equation $r \frac{\partial \tilde{u}}{\partial x} = -\frac{\partial(r\tilde{v})}{\partial r}$.

$$\left\{ \begin{array}{l} r \frac{\partial \tilde{u}}{\partial x} = r\omega_m i \exp(-i\omega_m t) F^2 \cos(\omega_m xF) \exp(\zeta_0 - i\Phi_0 - i\Phi_1^n) \\ = \exp(-i\omega_m t) \left[\begin{array}{l} -\left[G'(r) \cos(\omega_m xF) \exp(\zeta_0 - i\Phi_0 - i\Phi_1^n) \right] \\ +\omega_m xF' \sin(\omega_m xF) G(r) \exp(\zeta_0 - i\Phi_0 - i\Phi_1^n) \\ -\left(\zeta_0' - i\Phi_0' - i\Phi_1^{n'} \right) G(r) \cos(\omega_m xF) \exp(\zeta_0 - i\Phi_0 - i\Phi_1^n) \end{array} \right] \\ = -\frac{\partial(r\tilde{v})}{\partial r} \end{array} \right. \quad (4.29)$$

In the process we find the fundamental theorem of calculus, presented below,

$$\frac{d}{dx} \int_a^x f(t) dt = f(x) \quad (4.30)$$

to be essential for calculating the derivatives of ζ_0 , Φ_0 , and Φ_1^n with respect to r .

Accordingly, we have

$$\left\{ \begin{aligned}
\zeta'_0 &= \frac{d}{dr} \left(\xi \int_1^r \frac{x^3}{F^3(x)} dx \right) = \xi \frac{r^3}{F^3(r)} \\
\Phi'_0 &= \frac{d}{dr} \left(S \int_1^r \frac{x}{F(x)} dx \right) = S \frac{r}{F(r)} \\
\Phi_1^{n'} &= -\varepsilon S \frac{d}{dr} \left\{ (2n + \frac{3}{2}) [1 - r^2 F^{-2}(r)] \right. \\
&\quad \left. + (4n + 5) \int_1^r [x / F^2(x)] dx + 2\xi \int_1^r [x^5 / F^5(x)] dx \right\} \\
&= -\varepsilon S \left\{ (2n + \frac{3}{2}) [1 + 2r^2 F^{-3}(r) F'(r)] + 2 [r F^{-2}(r)] + 2\xi [r^5 F^{-5}(r)] \right\}
\end{aligned} \right. \quad (4.31)$$

We can simplify matters by recalling the WKB type I distinguished limit $S\sqrt{\varepsilon} = O(1)$,

which enables us to neglect higher order terms. $G(r)$ is readily calculated to be

$$G(r) = MF^3 \quad (4.32)$$

Returning to Eq. (4.28) and replacing G by its proper value, we extract the radial component of the velocity. Then by following Majdalani and Flandro (2002), we neglect the higher order acoustic radial component to obtain $v_1 = \tilde{v}$:

$$v_1 = \exp(-i\omega_m t) \left[\frac{1}{r} MF^3 \cos(\omega_m xF) \exp(\zeta_0 - i\Phi_0 - i\Phi_1^n) \right] \quad (4.33)$$

By retaining the dominant terms when differentiating Eqs. (4.27) and (4.33), the temporal vorticity is also obtained. We get

$$\Omega_1 = -\exp(-i\omega_m t) \left[S r \sin(\omega_m xF) \exp(\zeta_0 - i\Phi_0 - i\Phi_1^n) \right] \quad (4.34)$$

In the final assessment, the imaginary parts of Eqs. (4.27), (4.33), and (4.34) may be disregarded as only real components need to be retained for a meaningful expression. In summary, we retrieve

$$\begin{cases} u_1 = \sin(\omega_m x) \sin(\omega_m t) - F \sin(\omega_m x F) \exp(\zeta_0) \sin(\omega_m t + \Phi_0 + \Phi_1^n) \\ v_1 = \frac{1}{r} M F^3 \cos(\omega_m x F) \exp(\zeta_0) \cos(\omega_m t + \Phi_0 + \Phi_1^n) \\ \Omega_1 = S r \sin(\omega_m x F) \exp(\zeta_0) \cos(\omega_m t + \Phi_0 + \Phi_1^n) \end{cases} \quad (4.35)$$

Figure 4.1 has more to offer than just validating the favorable agreement between the type I axial velocity and its numerical counterpart. Not only does it display the role of the Strouhal and the injection Reynolds numbers in controlling the intensity of oscillations, it also exemplifies the importance of the viscous parameter εS^2 . Maintaining a constant penetration number $S_p = (\varepsilon S^2)^{-1} = R / S^2$ results in a constant penetration depth irrespective of the operating parameters. The presence of the no-slip condition is observed with the irrotational and solenoidal components of the wave canceling each other out at the wall's surface. On the other hand these components augment each other very close to the surface in what is known as the annular effect, first observed by Richardson and Tyler (1929). This phenomenon appears in porous tubes and channels in which fluid motion is rapidly alternating (Majdalani, 2009).

4.2 Near core approximations

Near the core, one can express the mean flow characteristic function as $F = \alpha r^2$, where $\alpha = (2, \frac{1}{2} \pi)$ can mimic, in that order, the small and large injection profiles as $r \rightarrow 0$.

4.2.1 WKB type I

The WKB type I solution, as $r \rightarrow 0$, alternates between zero, for odd orders of ε , and ∞ for even orders. This irregular behavior can be captured by carrying out the type I solution to higher orders while using the near core approximating function $F(r) = \alpha r^2$. This form will be appropriate, being representative of $F(r)$ in the region of non-uniformity. The procedure is identical to that followed in section 4.1.1, except that, only the real part of the dominant terms as $r \rightarrow 0$ will be considered. These alone dictate whether R_n^I approaches zero or infinity. The dominant terms for $S_0, S_1, S_2, \dots, S_7$ as $r \rightarrow 0$ may be determined asymptotically. They are given by

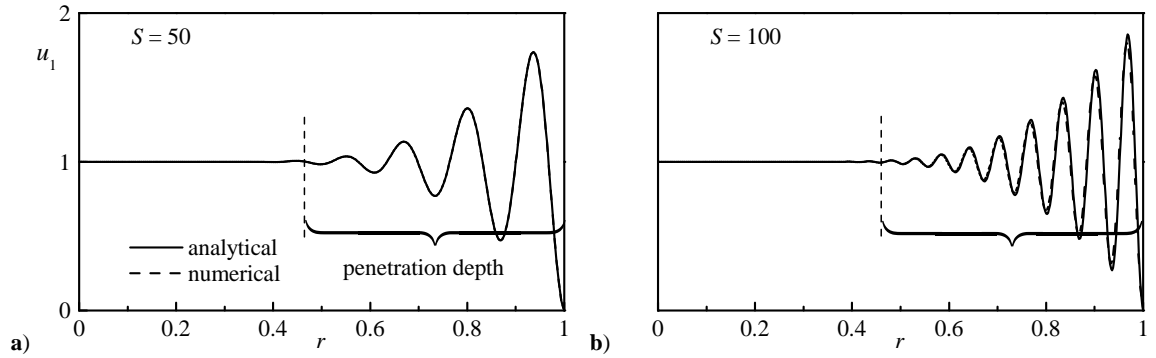


Figure 4.1. Numerical and analytical WKB type II solutions of the axially traveling wave for $F = \sin\left(\frac{1}{2}\pi r^2\right)$, $\varepsilon S^2 = 5$, $\omega_m t = \pi / 2$, $x / L = 0.5$, and a Strouhal number of a) $S = 50$ and b) $S = 100$. Fixing the penetration number $S_p = R / S^2 = 0.2$ results in a constant boundary layer thickness.

$$\begin{cases} S_0 = \frac{iS\sqrt{\varepsilon} \ln r}{\alpha}, & S_1 = -\frac{S^2\varepsilon}{2r^2\alpha^3}, & S_2 = -\frac{iS^3\varepsilon^{3/2}}{2r^4\alpha^5}, & S_3 = \frac{5S^4\varepsilon^2}{6r^6\alpha^7}, \\ S_4 = \frac{7iS^5\varepsilon^{5/2}}{4r^8\alpha^9}, & S_5 = -\frac{21S^6\varepsilon^3}{5r^{10}\alpha^{11}}, & S_6 = -\frac{11iS^7\varepsilon^{7/2}}{r^{12}\alpha^{13}}, & S_7 = \frac{429S^8\varepsilon^4}{14r^{14}\alpha^{15}} \end{cases} \quad (4.36)$$

A recurrence relation for the j^{th} term may hence be obtained, following Majdalani (2009):

$$S_j = C(j) \frac{(iS\sqrt{\varepsilon})^{j+1}}{2\alpha j(\alpha r)^{2j}}; \quad j \geq 1 \quad (4.37)$$

where the coefficients given by $C(j), j = 1, 2, \dots$ denote the Catalan numbers. These are defined by Abramowitz and Stegun (1964) in terms of a binomial ratio, specifically,

$$C(j) = \frac{(2j)!}{j!(j+1)!} \quad (4.38)$$

Note that these numbers were also discovered independently by Segner (Larcombe and French, 2000) and Majdalani (2009), the latter expressed them as

$$a_0 = 1, \quad a_{2j+1} = 2 \sum_{k=0}^{j-1} a_k a_{2j-k} + a_j^2, \quad j \geq 0; \quad a_{2j} = 2 \sum_{k=0}^{j-1} a_k a_{2j-k-1} + a_j^2, \quad j \geq 1 \quad (4.39)$$

4.2.2 WKB type II

For the WKB type II solution, the dominant terms at the core may be similarly obtained; however, the pattern at first glance is not as obvious as that in Eq. (4.36). To that end, more terms are retained to formulate a recursive formula. Furthermore, since the type II solution has two roots at every order, due to the quadratic nature of the Eikonal equation, only the terms retained in the regular type II analysis will be considered here. The Eikonal equation becomes

$$S_0 = \frac{\alpha^2 - \alpha\sqrt{\alpha^2 - 4iS\varepsilon} - 4iS\varepsilon \ln\left(2\sqrt{-iS\varepsilon}\right) + 4iS\varepsilon \ln\left(\alpha + \sqrt{\alpha^2 - 4iS\varepsilon}\right)}{4\alpha} \quad (4.40)$$

As for the higher order equations, we may put

$$\begin{cases} S_1 = -\frac{1}{2}\ln r, & S_2 = \frac{i\sqrt{-iS\varepsilon}}{8rS\varepsilon}, & S_3 = \frac{i}{16r^2S\varepsilon}, & S_4 = -\frac{25\sqrt{-iS\varepsilon}}{384r^3S^2\varepsilon^2}, \\ S_5 = -\frac{13}{128r^4S^2\varepsilon^2}, & S_6 = -\frac{1,073i\sqrt{-iS\varepsilon}}{5,120r^5S^3\varepsilon^3}, & S_7 = -\frac{103i}{192r^6S^3\varepsilon^3}, \\ S_8 = \frac{375,733\sqrt{-iS\varepsilon}}{22,9376r^7S^4\varepsilon^4}, & S_9 = \frac{23,797}{4,096r^8S^4\varepsilon^4}, & S_{10} = \frac{55,384,775i\sqrt{-iS\varepsilon}}{2,359,296r^9S^5\varepsilon^5} \end{cases} \quad (4.41)$$

with the above data, a recursive relation is formulated

$$S_j = a_j \left(\frac{i\sqrt{-i}}{r\sqrt{\varepsilon S}} \right)^{j-1}; \quad j \geq 2 \quad (4.42)$$

We find a_j to be a strictly positive constant. At the outset, Eq. (4.42) leads to a singularity pattern that may be expressed as

$$\begin{cases} S_j \rightarrow +\infty, & j \geq 1; & \text{whenever } \lfloor j/4 \rfloor \text{ is even} \\ S_j \rightarrow -\infty, & j \geq 0; & \text{whenever } \lfloor j/4 \rfloor \text{ is odd} \end{cases} \quad (4.43)$$

Table 4.3. Singularity pattern for the WKB type I and type II solutions

Type	Truncation Order									
	$O(\varepsilon)$	$O(\varepsilon^2)$	$O(\varepsilon^3)$...	$\lfloor j/4 \rfloor = 2\tau; \quad \tau \in \mathbb{N}$	$O(\varepsilon^{2j})$	$O(\varepsilon^{2j+1})$	$\lfloor j/4 \rfloor = 2\tau + 1$	$O(\varepsilon^{2j})$	$O(\varepsilon^{2j+1})$
I	0	∞	0	...	∞	0	∞	0	∞	0
II	∞	∞	∞	...	∞	∞	0	∞	0	0

where $\lfloor \cdot \rfloor$ denotes the Floor function. Furthermore, if we substitute the values for S_j into Eq. (4.22), we find that when $S_j \rightarrow \infty$ so will $R_n^{II} \rightarrow \infty$, and when $S_j \rightarrow -\infty$ we recover $R_n^{II} \rightarrow 0$. Table 4.3 summarizes the singularity pattern for both WKB solutions. For the type I solution near $r = 0$, the pattern is relatively simple: R_n^I alternates between 0 and ∞ with each successive order. Therefore, to obtain a uniformly valid behavior, the type I solutions should be truncated at odd orders in ε . This irregular behavior is also present in the type II solution. We find that as $r \rightarrow 0$, R_n^{II} switches from 0 to ∞ every four orders. This can be mathematically represented by taking the floor function $\lfloor \cdot \rfloor$ of the ratio $j / 4$. When this function is even, $R_n^{II} \rightarrow \infty$, and when it is odd, $R_n^{II} \rightarrow 0$. On this basis, the first uniformly valid behavior is realized at $O(\varepsilon^4)$. This is achieved by taking the first 5 terms in R_n^{II} , namely S_0, S_1, S_2, S_3 , and S_4 .

4.3 Matched asymptotic expansions

In order to overcome the core singularity associated with both type I and type II WKB solutions, the method of matched asymptotic expansions is pursued. This technique enables us to split the domain into an inner layer corresponding to the region of non-uniformity, and an outer region where the solution is well behaved. A suitable approximation is then constructed for each of these regions, and these local expansions are subsequently matched over their overlap segments before being combined into a composite solution that remains uniformly valid over the entire domain of interest.

4.3.1 Outer approximation

By suppressing all terms that involve the primary perturbation parameter ε in Eq. (3.25), our leading order inviscid outer solution may be obtained. This basic cancellation leaves us with

$$\frac{F}{r} \frac{dR_n^o}{dr} + \left[iS - 2(n+1) \frac{1}{r} F' \right] R_n^o = 0; \quad R_n^o(1) = 1 \quad (4.44)$$

where R_n^o refers to an outer expansion. As we suppress the term multiplying ε , the second order eigenfunction, Eq. (3.25), becomes a first order ODE, requiring only one of the two boundary conditions. The choice is straightforward, we disregard the boundary condition at the core, $R_n'(0) = 0$, and retain the meaningful condition at the wall, $R_n(1) = 1$. Being left with a well posed problem, Eq. (4.44) may be readily solved to obtain

$$R_n^o(r) = \sin\left(\frac{1}{2}\pi r^2\right)^{2+2n} \tan\left(\frac{1}{4}\pi r^2\right)^{-iS/\pi} \quad (4.45)$$

To segregate the contribution of the outer solution in the core region, we take the limit as $r \rightarrow 0$. This operation renders the inner expansion of the outer solution, otherwise known as $(R_n^o)^i$:

$$(R_n^o)^i = 2^{iS/\pi} \left(\frac{1}{2}\pi r^2\right)^{2+2n-iS/\pi} \quad (4.46)$$

The determination of a compact outer solution will prove to be instrumental in retrieving an expression for the inner expansion. This aspect will be illustrated next.

4.3.2 Inner core approximation

Near the core, one can express the mean flow characteristic function as $F = \alpha r^2$, where $\alpha = \frac{1}{2}\pi$ mimics the large injection profile, $F = \sin\left(\frac{1}{2}\pi r^2\right)$, used for the outer solution as $r \rightarrow 0$. Equation (3.25) can then be subjected to a double variable transformation of the type

$$\begin{cases} \chi = r\sqrt{\pi / 2\varepsilon} \\ R_n^i(\chi) = f(\chi) \exp\left(-\frac{1}{4}\chi^2\right) \end{cases} \quad (4.47)$$

At the outset, the rescaled Eq. (3.25) becomes

$$\frac{d^2f}{d\chi^2} + \frac{1}{\chi} \frac{df}{d\chi} + \left(-5 - 4n - \frac{1}{4}\chi^2 + 2i\frac{S}{\pi}\right)f = 0; \quad \frac{df(0)}{d\chi} = 0 \quad (4.48)$$

Note that only the boundary condition in the core region is transformed. The second boundary condition must be evaluated in the far field to the extent of reproducing the inner expansion of the outer solution, $(R_n^o)^i$. Equation (4.48) may be readily manipulated to produce

$$f(\chi) = c_0 \sqrt{2} \exp\left(\frac{1}{4}\chi^2\right) L_\eta\left(-\frac{1}{2}\chi^2\right); \quad \eta = 2 + 2n - iS / \pi \quad (4.49)$$

where c_0 is a constant that must be determined through a matching operation that ensures the seamless blending of the inner and outer solutions in their overlap regions. In the above, the special function $L_y(x)$ represents the Laguerre polynomial. It is defined in terms of $\Phi(a, b, x)$, the Kummer function of the first kind (Abramowitz and Stegun, 1964). These functions are given by

$$L_y(x) = \exp(x)\Phi(y+1, 1, -x) \quad (4.50)$$

and

$$\Phi(a, b, x) = \sum_{k=0}^{\infty} \frac{a_k}{b_k} \frac{z^k}{k!} \quad (4.51)$$

At this stage, Prandtl's matching principle may be implemented. Accordingly, the inner limit of the outer solution $(R_n^o)^i$ must be equated to the outer limit of the inner solution $(R_n^i)^o$. Finding the latter requires the use of the large x approximation of the Kummer function Φ ,

$$\Phi(a, b, x) = \frac{\Gamma(b)}{\Gamma(a)} \exp(x)x^{a-b} \left[1 + \mathcal{O}(x^{-1}) \right]; \quad x \rightarrow \infty \quad (4.52)$$

This expression enables us to convert Eq. (4.49) into

$$\left\{ \begin{aligned} f(\chi) &= c_0 \sqrt{2} \Phi(3 + 2n - iS / \pi, 1, \frac{1}{2} \chi^2) \\ &\sim \frac{c_0 \sqrt{2} \Gamma(1)}{\Gamma(3 + 2n - iS / \pi)} \exp(\frac{1}{2} \chi^2) \left(\frac{1}{2} \chi^2 \right)^{2+2n-iS/\pi} \end{aligned} \right. \quad (4.53)$$

whence, based on Eq. (4.47),

$$(R_n^i)^o = \lim_{\chi \rightarrow \infty} f(\chi) \exp\left(-\frac{1}{4} \chi^2\right) \quad (4.54)$$

which in terms of r , becomes

$$(R_n^i)^o = \frac{c_0 \sqrt{2}}{\Gamma(3 + 2n - iS / \pi)} \exp\left(\frac{\pi r^2}{8\varepsilon}\right) \left(\frac{\pi r^2}{4\varepsilon}\right)^{2+2n-iS/\pi} \quad (4.55)$$

Solving for c_0 by equating $(R_n^i)^o$ to $(R_n^o)^i$ gives

$$c_0 = \frac{2^{iS/\pi} \left(\frac{1}{2} \pi r^2\right)^{2+2n-iS/\pi}}{\sqrt{2} \Gamma^{-1} \left(3 + 2n - iS / \pi\right) \left(\frac{1}{4} \pi r^2 \varepsilon^{-1}\right)^{2+2n-iS/\pi}} \quad (4.56)$$

Equation (4.56) may be further simplified to yield

$$c_0 = \sqrt{2} \Gamma \left(3 + 2n - iS / \pi\right) 2^{1+2n} \varepsilon^{2+2n-iS/\pi} \quad (4.57)$$

Switching back to Eq. (4.49), the inner solution at order ε returns

$$R_n^i(r) = 2^{iS/\pi} (2\varepsilon)^{2+2n-iS/\pi} \Gamma \left(3 + 2n - iS / \pi\right) L_\eta \left(-\pi r^2 / 4\varepsilon\right) \quad (4.58)$$

The net inner correction, $R_n^{ni} = R_n^i - (R_n^i)^o$, is thus at hand. R_n^{ni} denotes the correction that must be added to the outer solution to overcome its irregular behavior near $r = 0$.

The net inner correction reads

$$R_n^{ni}(r) = \Gamma \left(3 + 2n - iS / \pi\right) 2^{2+2n} \varepsilon^{2+2n-iS/\pi} L_\eta \left(-\frac{1}{4} \pi R r^2\right) - 2^{iS/\pi} \left(\frac{1}{2} \pi r^2\right)^{2+2n-iS/\pi} \quad (4.59)$$

The net inner correction adjusts the value of the outer domain solution near the core, and should asymptote to zero as it approaches the outer boundary. However, because in the process of obtaining an inner solution, an approximate test function $F(r) = \frac{1}{2} \pi r^2$ had to be used to arrive at a closed form analytic solution, the net inner correction carries with it a small asymptotic residue away from the centerline. This residue is strongly dependent on how ε and S scale.

Figure 4.2 delineates the behavior of R_n^{ni} as we fix the Strouhal number and allow the crossflow Reynolds number to vary. It is clear that for a fixed Strouhal number, the wiggles observed in R_n^{ni} away from the core diminish as R increases. On the other

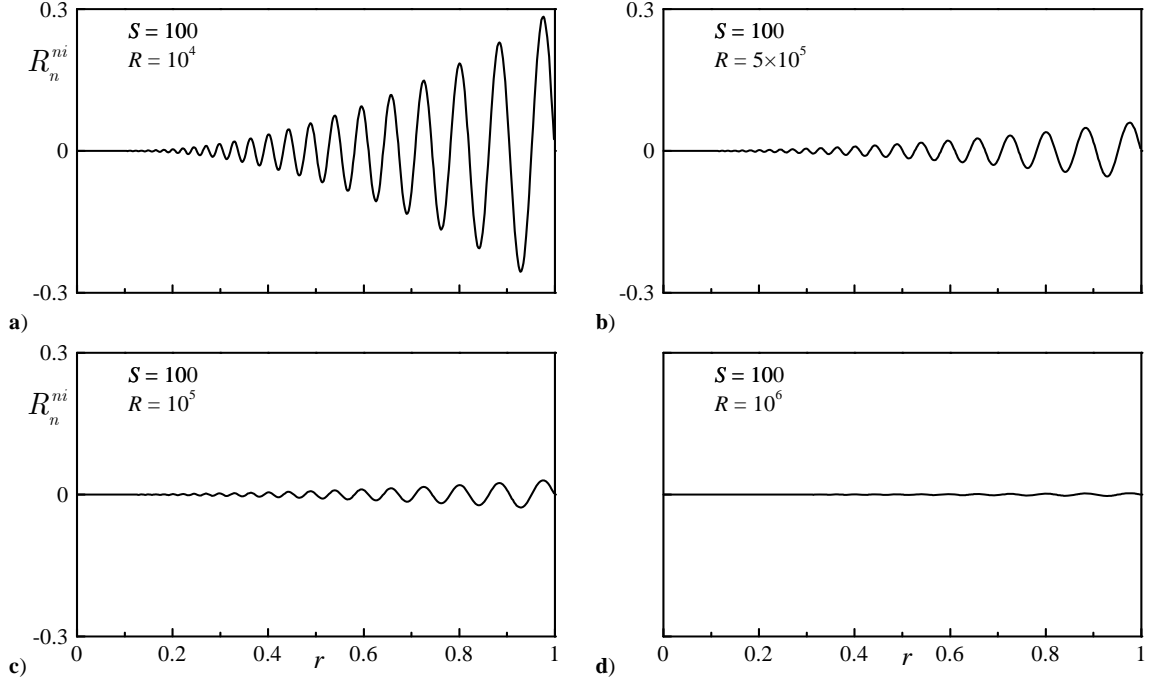


Figure 4.2. Residue error in the net inner correction away from the centerline. The value of the Strouhal number is kept constant as we allow the crossflow Reynolds number to vary. Four cases are considered: a) $R = 10^4$, b) 5×10^4 , c) 10^5 , and d) 10^6 . Evidently, the larger the crossflow Reynolds number, the smaller the residue.

hand, referring to Figure 4.3, it is evident that an increase in the Strouhal number reflects negatively on E_{\max}^{ni} , the maximum absolute error of R_n^{ni} . Here E_{\max}^{ni} represents the maximum amplitude of the residue depicted in Figure 4.2, it is given by:

$$E_{\max}^{ni} = \max \left| R_n^{ni} \right|; \quad 0 \leq r \leq 1 \quad (4.60)$$

For the Strouhal and Reynolds number values used in Figure 4.2a, $E_{\max}^{ni} \approx 0.3$.

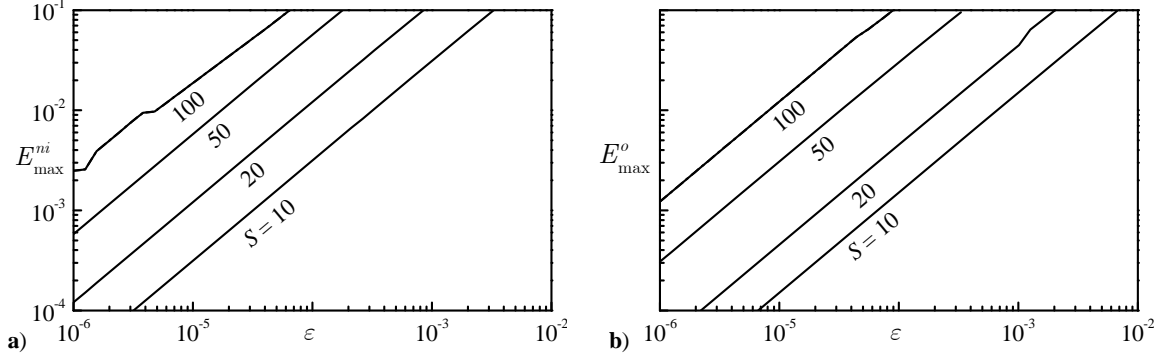


Figure 4.3 Asymptotic behavior of a) E_{\max}^{ni} , and b) E_{\max}^o . Four values of the Strouhal number are considered: $S = 10, 20, 50,$ and 100 .

At this point, a composite solution may be constructed by adding R_n^{ni} to the outer inviscid solution R_n^o . Despite the inability to incorporate viscous corrections into the outer expansion, the composite solution is seen to capture some viscous effects by virtue of the net inner correction.

Figure 4.3 shows two curves that portray a) the inherent error in the net inner correction resulting from the use of a near core approximating function $F = \alpha r^2$, and b) the error, E_{\max}^o , associated with the inviscid outer solution. The latter is a measure of the maximum difference between R_n^o and the leading order WKB type I solution R_n^I , in which viscous effects are accounted for; it may be expressed as:

$$E_{\max}^o = \max \left| \sin\left(\frac{1}{2}\pi r^2\right)^{2+2n} \tan\left(\frac{1}{4}\pi r^2\right)^{-iS/\pi} - F^{2n+2} \exp\left(\zeta_0 - i\Phi_0 - i\Phi_1^n\right) \right| \quad (4.61)$$

Table 4.4. Numerical and asymptotic solutions using $S = 10$, $R = 10^3$, $n = 0$, and $F = \sin\left(\frac{1}{2}\pi r^2\right)$

r	<u>WKB I</u>	<u>WKB II</u>	<u>Numerical</u>	<u>Composite</u>
0.00	∞	∞	1.37×10^{-6}	1.39×10^{-6}
0.05	∞	-0.000014	-0.000014	-0.000014
0.10	-0.000259	0.000018	0.000017	0.000020
0.15	0.000998	0.000907	0.000908	0.000924
0.20	-0.001189	-0.001189	-0.001188	-0.001264
0.25	-0.008467	-0.008424	-0.008425	-0.008614
...				
0.75	-0.418811	-0.418824	-0.418824	-0.413059
0.80	-0.223137	-0.223143	-0.223143	-0.205649
0.85	0.115410	0.115411	0.115411	0.143387
0.90	0.517774	0.517780	0.517780	0.550385
0.95	0.857983	0.857989	0.857989	0.885910
1.00	1.000000	1.000000	1.000000	1.013719

Moreover, as depicted in Figure 4.3, the relatively small error E_{\max}^o associated with neglecting viscosity in R_n^o is always less than the inbuilt error related to the net inner correction, thus justifying the use of R_n^o in the composite solution.

4.3.3 The composite solution

Our composite solution is formed by superimposing the net inner correction and the outer solution. One obtains

$$R_n^c = R_n^{mi} + R_n^o \quad (4.62)$$

A comparison between the second-order asymptotic approximations and highly accurate numerical predictions is presented in Table 4.4. By looking at the domain's

endpoints, it is interesting to see how well the composite approximation matches the numerical value at the origin. Meanwhile, both types of WKB expansions fail to a certain degree by providing either a vanishingly small or an infinitely large magnitude as $r \rightarrow 0$. Nonetheless, as we move away from the origin, the WKB approximations begin to outperform, as they should, the composite expansion from which the outer solution may be recovered only asymptotically in ε . Thus unless ε is exceedingly small, the ability of the composite solution to outperform the outer solution in the outer region will remain limited. This explains the small discrepancy in the composite approximation near $r = 1$, a weakness to which the WKB solutions are immune.

4.4 Special case of an exact solution

We have seen so far that the case of $F = \alpha r^2$, where $\alpha = (2, \frac{1}{2}\pi)$, can asymptotically reproduce, when expanded near the core, the small and large injection solutions, respectively. In addition to the role that it serves in constructing a near-core approximation, the characteristic function itself leads to an exact solution across the entire solution interval. This can be readily achieved using the dual variable transformations,

$$\begin{cases} \chi = r\sqrt{\alpha/\varepsilon} \\ R(\chi) = \exp(-\frac{1}{4}\chi^2)f(\chi) \end{cases} \quad (4.63)$$

Equation (3.25) and its two boundary conditions simplify into

$$\frac{d^2 f}{d\chi^2} + \frac{1}{\chi} \frac{df}{d\chi} + \left(iS\alpha^{-1} - 5 - 4n - \frac{1}{4}\chi^2 \right) f = 0; \begin{cases} \frac{df(0)}{d\chi} = 0 \\ f\left(\sqrt{\alpha/\varepsilon}\right) = \exp\left(\frac{1}{4}\alpha/\varepsilon\right) \end{cases} \quad (4.64)$$

This enables us to extract an exact solution to this set, namely,

$$f(\chi) = \frac{L_\theta\left(-\frac{1}{2}\chi^2\right)}{L_\theta\left(-\frac{1}{2}\alpha R\right)} \exp\left(\frac{1}{4}\chi^2\right); \quad \theta = 2 + 2n - \frac{1}{2}iS\alpha^{-1} \quad (4.65)$$

Reverting back to the original variables, we get

$$R_n^E(r) = \frac{L_\theta\left(-\frac{1}{2}\alpha Rr^2\right)}{L_\theta\left(-\frac{1}{2}\alpha R\right)} = \frac{\Phi\left(1 + \theta, 1, \frac{1}{2}\alpha r^2 R\right)}{\Phi\left(1 + \theta, 1, \frac{1}{2}\alpha R\right)} \exp\left[\frac{1}{2}\alpha R(1 - r^2)\right] \quad (4.66)$$

where the superscript ‘E’ denotes an exact outcome. For the two cases at hand, Eq.

(4.66) leads to

$$R_n^E(r) = \begin{cases} \frac{L_\eta\left(-\frac{1}{4}\pi Rr^2\right)}{L_\eta\left(-\frac{1}{4}\pi R\right)}; & \alpha = \frac{1}{2}\pi, \quad \eta = 2 + 2n - iS/\pi \\ \frac{L_\mu\left(-Rr^2\right)}{L_\mu\left(-R\right)}; & \alpha = 2, \quad \mu = 2 + 2n - iS/4 \end{cases} \quad (4.67)$$

In Table 4.5, $R_n^E(r)$ is compared to the numerical and WKB approximations for $F = \frac{1}{2}\pi r^2$ and a typical set of physical parameters. Based on the data entries, it may be surmised that the exact and numerical solutions agree perfectly well, as they should, over the entire domain. As for the asymptotic expressions, they agree with the true values everywhere except at the centerline where they either vanish (type I), thus missing the small asymptotic value at $r \rightarrow 1$, or grow unbounded (type II), thus requiring a local matched asymptotic treatment.

Table 4.5. Numerical, exact, and asymptotic solutions at $O(\varepsilon)$ for $S = 20$,
 $R = 10^3$, $n = 0$, and $F = \frac{1}{2}\pi r^2$

r	<u>WKB I</u>	<u>WKB II</u>	<u>Numerical</u>	<u>Exact</u>
0.00	0	∞	-1.21×10^{-8}	-1.21×10^{-8}
0.05	0	-1.47×10^{-7}	-1.53×10^{-8}	-1.53×10^{-8}
0.10	-6.03×10^{-7}	9.52×10^{-6}	9.27×10^{-6}	9.27×10^{-6}
0.15	-0.000054	-0.000106	-0.000114	-0.000114
0.20	0.000382	0.000458	0.000483	0.000483
0.25	-0.000395	-0.000384	-0.000365	-0.000365
...				
0.75	-0.267450	-0.267661	-0.268683	-0.268683
0.80	-0.377773	-0.377978	-0.379073	-0.379073
0.85	-0.238870	-0.238956	-0.239463	-0.239463
0.90	0.152272	0.152298	0.152445	0.152445
0.95	0.645061	0.645114	0.645456	0.645456
1.00	1.000000	1.000000	1.000000	1.000000

4.5 Numerical Solution

Despite the unsuspecting, deceptively simple form of Eq. (3.25), its numerical solution presents its own challenges. First, the role of ε multiplying the highest derivative leads to numerical instability that is aggravated by successive increases in R . Thus for a given ε , a maximum step size cannot be exceeded lest spurious results are obtained. Second, the r^{-1} factors that affect several members of the integrands pose additional singularities in the vicinity of $r = 0$. Third, extracting the real component of the total wave after summation needs to be carefully performed. To illustrate how the solution may be entirely carried out in the real domain, we introduce the inverse transformation

$$g(r, t) = R_n(r)e^{-iT}, \quad T = \omega_m t \quad (4.68)$$

with

$$\frac{\partial g}{\partial r} = R'_n(r)e^{-iT}, \quad \frac{\partial^2 g}{\partial r^2} = R''_n(r)e^{-iT}, \quad \frac{\partial g}{\partial T} = -iR_n(r)e^{-iT} \quad (4.69)$$

These expressions may be substituted into Eq. (3.25) and simplified through multiplication by e^{-iT} . An equivalent PDE emerges, namely,

$$\varepsilon \frac{\partial^2 g}{\partial r^2} + \frac{1}{r}(F + \varepsilon) \frac{\partial g}{\partial r} - \frac{2}{r}(n + 1)F'g = S \frac{\partial g}{\partial T} \quad (4.70)$$

The boundary conditions in Eq. (3.25) may be similarly converted via Eq. (4.68). One gets

$$\begin{cases} g(1, t) = e^{-iT} \\ \frac{\partial g}{\partial r}(0, t) = 0 \end{cases} \quad (4.71)$$

Given harmonic oscillations in time, our PDE in Eq. (4.70) may be conveniently reduced to a coupled set of ODEs by setting

$$g(r, t) = g_1(r) \sin T - g_2(r) \cos T \quad (4.72)$$

Consequently, the linear, second-order set in (g_1, g_2) is arrived at:

$$\begin{cases} g_1'' = \left[\frac{2}{r}(n + 1)F'g_1 - \frac{1}{r}(F + \varepsilon)g_1' + Sg_2 \right] R \\ g_2'' = \left[\frac{2}{r}(n + 1)F'g_2 - \frac{1}{r}(F + \varepsilon)g_2' - Sg_1 \right] R \end{cases} \quad (4.73)$$

This system can be numerically integrated given the following assortment of auxiliary conditions

$$\begin{cases} g_1(1) = -i, & g_2(1) = -1 \\ g_1'(0) = 0, & g_2'(0) = 0 \end{cases} \quad (4.74)$$

Once a solution is achieved, the wave motion can be reproduced using

$$\begin{cases} u_1 = \sin(\omega_m x) \sin(\omega_m t) + i \sin(\omega_m x) \cos(\omega_m t) \\ -i \sum_{n=0}^{\infty} (-1)^n \frac{(\omega_m x)^{2n+1}}{(2n+1)!} (g_1 \sin \omega_m t - g_2 \cos \omega_m t) \end{cases} \quad (4.75)$$

where only the real part is meaningful. The axially traveling wave can be extracted from

$$u_1 = \sin(\omega_m x) \sin(\omega_m t) - \sum_{n=0}^{\infty} (-1)^n \frac{(\omega_m x)^{2n+1}}{(2n+1)!} \Re \left[i (g_1 \sin \omega_m t - g_2 \cos \omega_m t) \right] \quad (4.76)$$

or, equivalently, letting $f_1(r) = \Re[i g_1(r)]$, $f_2(r) = \Re[i g_2(r)]$, one gets the equivalent problem cast in the real domain

$$u_1 = \sin(\omega_m x) \sin(\omega_m t) - \sum_{n=0}^{\infty} (-1)^n \frac{(\omega_m x)^{2n+1}}{(2n+1)!} (f_1 \sin \omega_m t - f_2 \cos \omega_m t) \quad (4.77)$$

such that f_1 and f_2 may be retrieved directly from the real ODEs

$$\begin{cases} f_1'' = \left[\frac{2}{r} (n+1) F' f_1 - \frac{1}{r} (F + \varepsilon) f_1' + S f_2 \right] R \\ f_2'' = \left[\frac{2}{r} (n+1) F' f_2 - \frac{1}{r} (F + \varepsilon) f_2' - S f_1 \right] R \end{cases} \quad \begin{cases} f_1(1) = 1, & f_2(1) = 0 \\ f_1'(0) = 0, & f_2'(0) = 0 \end{cases} \quad (4.78)$$

In summary, it is sufficient to solve Eq. (4.78) and substitute the results into Eq. (4.77) to deduce the wave form at any instant of time.

Chapter 5 Results and Discussion

Inasmuch as this problem resembles its porous channel flow analog, mathematically it is quite different. For the cylindrical geometry, the r^{-1} term multiplying the R'_n in (3.25) changes the character of the differential equation, thus making it more difficult to produce a near core approximation. Furthermore, it is interesting to note that in the channel case, the singularity at the core is associated with the WKB type I solution while the type II solution remains uniformly valid throughout the entire domain. This situation becomes more complex in a cylindrical geometry. On the one hand, the type I approximation exhibits the expected singularity at every other order in ε with a pattern that is identical to its Cartesian counterpart. On the other hand, the type II solution, once uniformly valid for the channel case, now exhibits a singularity pattern that is highly dependent on the truncation order.

Away from the core, the WKB solutions are well behaved and accurate. However, their inherent singularity at the centerline must be carefully treated. In this study, matched asymptotic expansions are used to arrive at a uniformly valid composite solution capable of capturing the small amplitude wave velocity at the centerline. Nevertheless, the increased accuracy associated with the composite solution at the core comes at the expense of a small residual error plaguing the outer expansion. In the

process of formulating a composite solution, an inner core test function $F = \frac{1}{2}\pi r^2$ had to be used to arrive at a closed form analytical solution. Even though the test function is an excellent approximation near the core, it becomes the source of discrepancy in the outer domain. At the outset, we now have a choice between two methods of analytical solutions, one that is highly accurate away from the center (WKB solutions) but fails to capture the behavior of the wave around the core, and another (composite solution), which excels where the WKB fails, but falls short where the WKB approximation performs superbly well, away from the centerline. Depending on what region of the domain is of interest, near core or outer domain, one may decide on one method over the other, or ultimately both, each in their respective region.

Examining Figures 5.1 and 5.2, the physical significance of the WKB type I and type II distinguished limits may be inferred. When the variables are such that $\varepsilon S^2 = \text{const}$, (for the type I distinguished limit, $S^2 = O(R)$) and S is larger than some critical, relatively small value, a fixed penetration depth is achieved irrespective of the amplitude of each variable taken separately. Moreover, for an increase or decrease in the size of RS , the frequency of the wave is either elevated or reduced, respectively. On the other hand, when ε and S scale according to $\varepsilon S = \text{const}$, (for the type II distinguished limit, $S = O(R)$) the pattern observed projects an increase in the wave intensity accompanied by a decrease in the penetration depth when RS increases. The exact opposite behavior is observed for a reduction in RS .

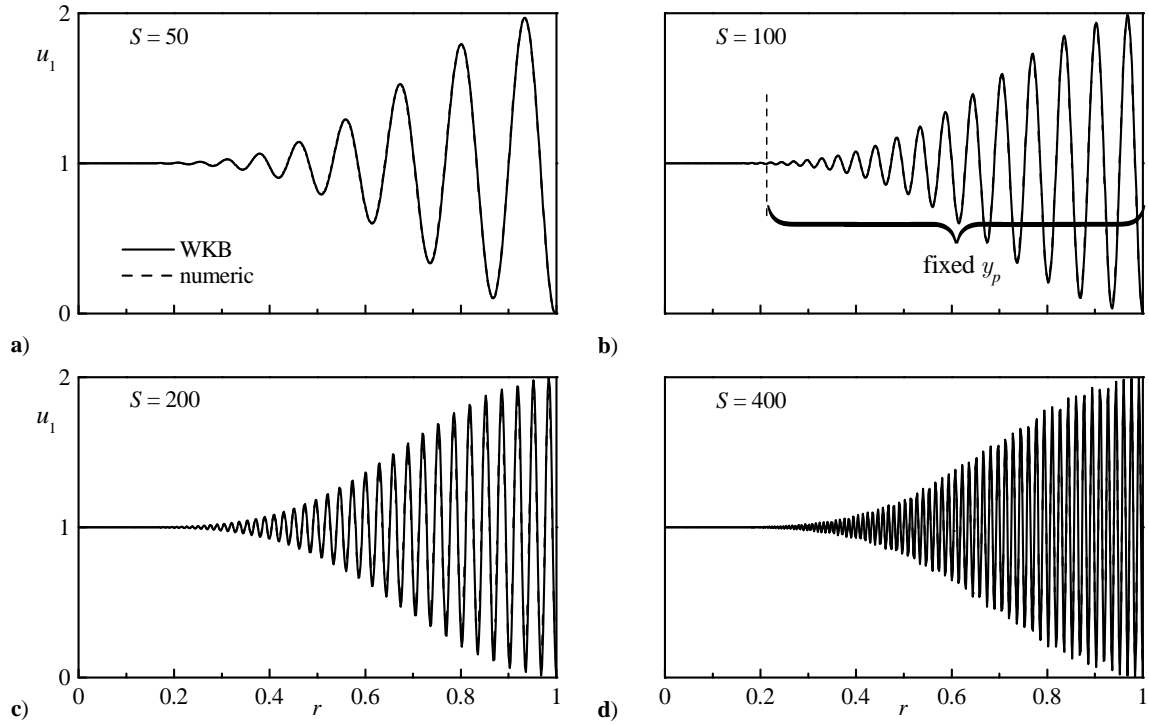


Figure 5.1. Analytical (WKB type II) and numerical solutions of the axially traveling wave for $F = \sin\left(\frac{1}{2}\pi r^2\right)$, $S_p = 5$, $m = 1$, $\omega_m t = \pi/2$, $x/l = 0.5$, and a Strouhal number of: a) $S = 50, 100, 200$, and 400 . With a fixed penetration number, the penetration depth y_p remains constant regardless of the wall injection velocity or frequency of oscillations. Despite the wave's increased spatial frequency, the agreement between numerics and asymptotics seems excellent.

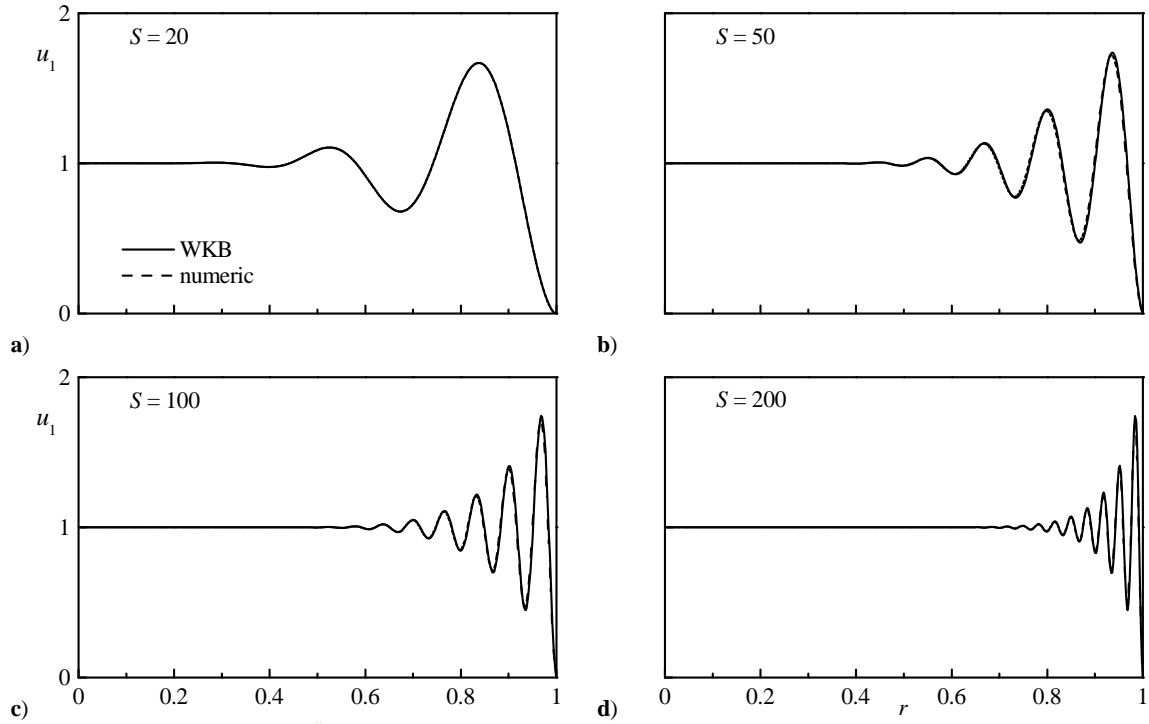


Figure 5.2 Analytical (WKB type II) and numerical solutions of the axially traveling wave for $F = \sin\left(\frac{1}{2}\pi r^2\right)$, $\varepsilon S = 0.1$, $m = 1$, $\omega_m t = \pi / 2$, $x / l = 0.5$, and a Strouhal number of: a) $S = 20$, 50, 100, and 200. When ε and S scale according to $\varepsilon S = \text{const}$, the pattern observed is an increase in the wave intensity accompanied by a decrease in the penetration depth when the value of SR increases. Here, the analytical solution is a mirror image of its numerical counterpart.

Figure 5.3a shows how the penetration depth of the wave varies as the crossflow Reynolds number and the Strouhal number change. When R is held fixed, the penetration depth is decreased as S is increased. Moreover, as the Strouhal number gets larger, the sensitivity of the penetration depth to R is amplified. Conversely, Figure 5.3b depicts the variation in the penetration depth for different values of ξ . A constant penetration depth y_p is achieved when ξ is held constant; however, S must be above some minimum value dictated by the magnitude of the penetration number $S_p = R / S^2$. The reason for the penetration depth being always larger at somewhat lower Strouhal numbers is that the wave would have relatively lower frequencies in those situations, a condition that allows it to spatially delay its asymptotic approach to zero, thus leading to a larger penetration depth. On the contrary, when εS is held constant in Figure 5.3c, y_p diminishes as S increases. Furthermore, Figure 5.3d illustrates the dependency and sensitivity of y_p on S_p . When S_p falls in the range $0.02 \leq S_p \leq 1$, the changes in y_p are most significant when compared to variations outside that domain. In fact, when S_p jumps from 0.02 to 1, the penetration depth expands by as much as 56% covering 15% of the tube's radius at $S_p = 0.02$ to about 71% at $S_p = 1$. Beyond $S_p = 1$, namely $1 \leq S_p \leq 100$, y_p spreads out an additional 9% reaching a maximum value of 80% at $S_p = 100$. In fact, the penetration depth begins to plateau for penetration numbers

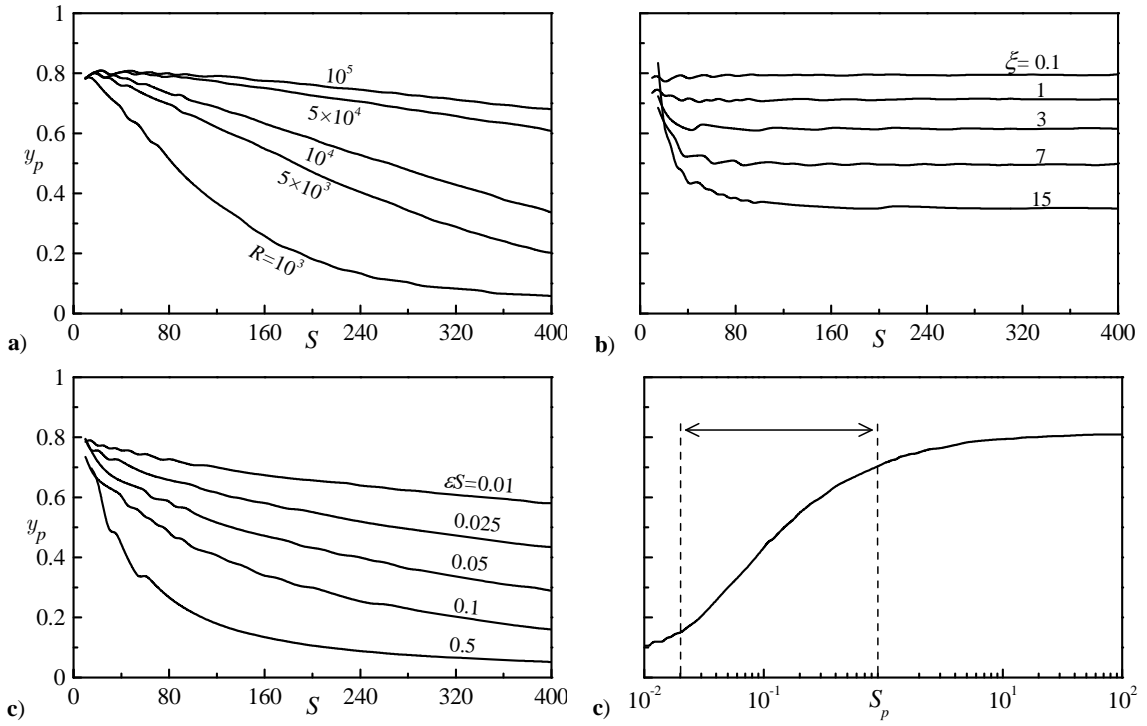


Figure 5.3 a) Penetration depth y_p vs S for multiple values of R . When R is held constant, y_p decreases with higher frequencies. Also the sensitivity of y_p on S is amplified at large Strouhal numbers; b) y_p vs S for multiple values of ξ . Note that y_p remains constant when ξ is fixed and S is increased above a critical, relatively small, value. c) y_p vs S for multiple values of εS . Unlike case b, y_p diminishes as εS is increased. d) y_p vs S_p , y_p is most susceptible to change when $0.02 \leq S_p \leq 1$.

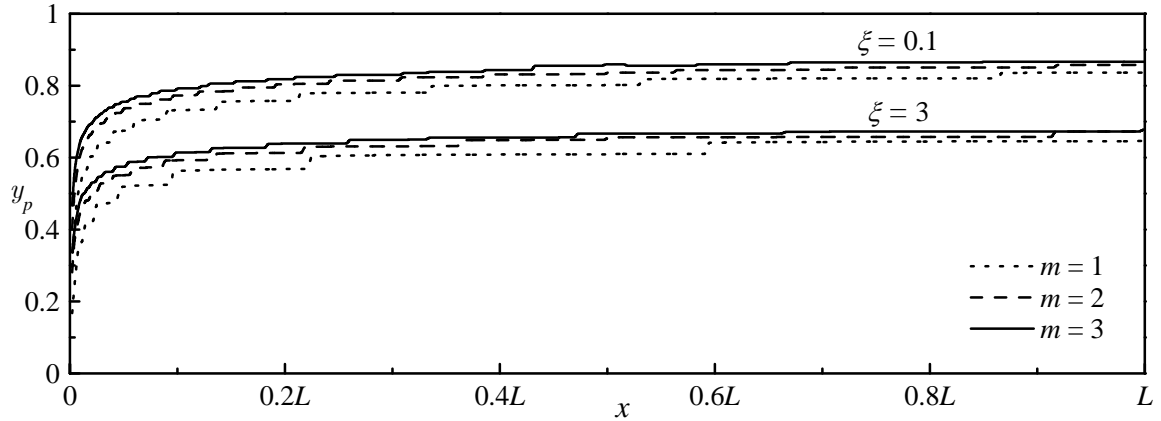


Figure 5.4 Penetration depth vs x for $S = 100$, $m = 1, 2, 3$ with $\xi = 0.1$ and 3 .

Only the mode number is allowed to change, while ξ is kept constant.

beyond $S_p = 1$. A more detailed study on the penetration depth is carried out by Majdalanin (1999a).

Figure 5.4 depicts the penetration depth as the velocity wave progresses through the tube. Close to the headwall, the wave is still developing which results in a small penetration depth. The wave quickly develops as it propagates away from the headwall; in fact, before reaching 10% of the tube's length, the penetration depth becomes more than 90% of its maximum; that maximum is located at the tube's end. When ξ is held constant, the depth of the wave is shown to be slightly widened throughout the tube as the mode number is increased. Moreover, y_p slightly increases as the wave propagates towards the downstream end because of the boundary layer being convected by the mean flow towards the tube's end. If we take the special case of $m = 1$ midway through the

tube, we find that $y_p \approx 0.6$ for $\xi = 3$, and $y_p \approx 0.8$ for $\xi = 0.1$. These values are in excellent agreement with the results obtained in Figure 5.3.

So far we have only sketched the velocity wave at a single location in the tube, midway between both ends, and for one oscillation mode number $m = 1$. Figure 5.5 illustrates the behavior of the wave throughout the entire tube for multiple mode numbers. When the oscillation mode number is increased, the magnitude of $u_1(x, r, t)$ appears to follow the spatial mode shape of the irrotational component of the wave

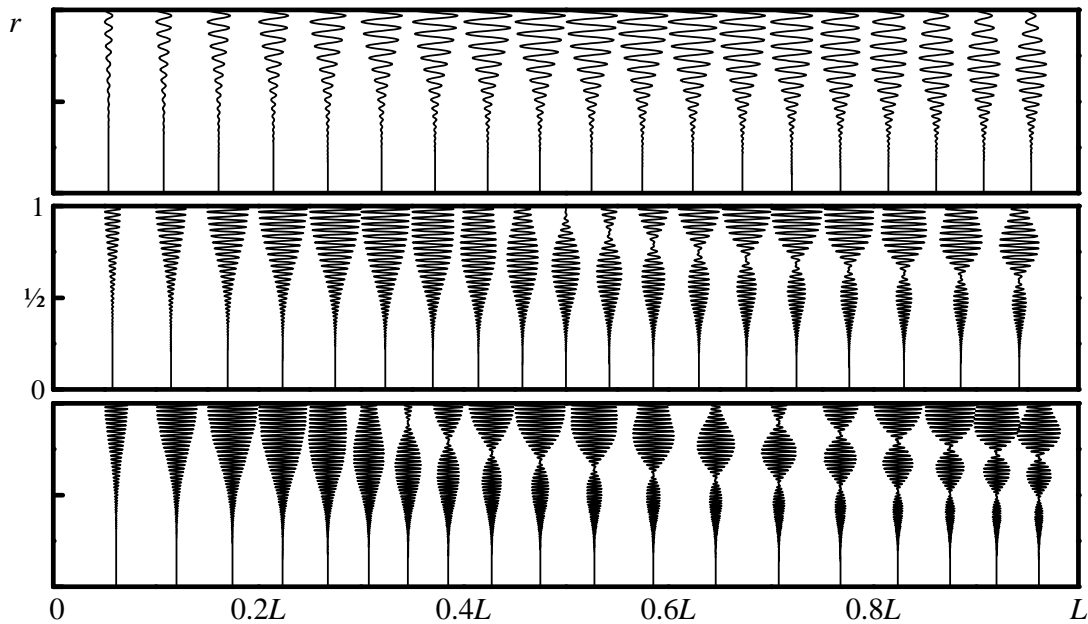


Figure 5.5 WKB type II modulus of the time-dependent velocity $u_1(x, r, t)$ for the first three oscillation modes. Results are shown at equal intervals along the tube. Here $R = 10^4$ and $S = 100m$ with $m = 1, 2, 3$.

embodied in the first part of Eq. (3.26). For the first mode, the magnitude of the wave grows from a minimum at the tube's head end to a maximum midway along the cylinder where the modulus of the sinusoidal wave is largest. The penetration depth of the wave, for any mode, continues to increase along the tube as a result of the convection of the unsteady vorticity. When higher mode numbers are considered, $m \geq 2$, we notice the presence of velocity nodes, points where the velocity magnitude vanishes. The number and location of these nodes depends on the mode number and are described in a technical note by Majdalani (1999a).

Chapter 6 Conclusions and Recommendations

This study investigates the behavior of a uniform Newtonian flow subjected to small pressure oscillations in a cylindrical tube with injecting sidewall. Particular to this investigation, two forms of WKB approximations are derived and presented to arbitrary order. These analytical solutions are in good agreement with numerical data especially in the outer domain, but fail to capture the small wave amplitude at the centerline. Both types display a pattern of singularity at the core, obtained through a near core approximation study, that alternates between zero and infinity, depending on the order of truncation. However, through a series of transformations, matched asymptotic expansions are used to develop a composite, singularity free approximation valid over the entire domain. The composite solution achieved three goals: (a) it overcame the inherent singularity associated with the WKB solutions near $r = 0$; (b) it confirmed, to several decimal places, the calculated numerical value at the centerline; (c) it demonstrated Prandtl's principle of matching with supplementary expansions. Nonetheless, the accuracy of the composite solution comes at the expense of reduced precision in the outer field. Both WKB II and matched asymptotic expansions of this problem represent novel and essential solutions of the long standing problem involving axially traveling waves in porous cylinders.

Future investigators should examine other methods for deriving the composite solution. While R_n^c matches the numerical solution persistently to several decimal places at the centerline, it loses accuracy as it approaches the tube's wall. The flowfield in the porous chamber arises solely from injection at the sidewall; no headwall injection is considered. Moreover, an oscillatory pressure wave sweeping the cylinder along its longitudinal axis is superimposed on the mean flow. A similar study for interested researchers might be to examine the flowfield with, for example, a Berman injection profile at the headwall while excluding sidewall injection. For that case, one could consider a transverse pressure wave that travels both radially and tangentially along the tube's circumference.

References

References

- Bender, C. M. and S. A. Orszag (1978). Advanced Mathematical Methods for Scientists and Engineers. New York, McGraw-Hill.
- Abramowitz, M., Stegun, I.A., 1964. Handbook of Mathematical Functions, National Bureau of Standards, New York.
- Beddini, R.A., Roberts, T.A., 1992. Response of propellant combustion to a turbulent acoustic boundary layer. *Journal of Propulsion and Power* 8, 290-296.
- Bender, C.M., Orszag, S.A., 1978. *Advanced Mathematical Methods for Scientists and Engineers*, McGraw-Hill, New York.
- Berman, A.S., 1953. Laminar flow in channels with porous walls. *Journal of Applied Physics* 24, 1232-1235.
- Brady, J.F., Acrivos, A., 1981. Steady flow in a channel or tube with an accelerating surface velocity. An exact solution to the Navier-Stokes equations with reverse flow. *Journal of Fluid Mechanics* 112, 127-150.
- Culick, F.E.C., 1966. Rotational axisymmetric mean flow and damping of acoustic waves in a solid propellant rocket. *AIAA Journal* 4, 1462-1464.
- Dunlap, R., Blackner, A.M., Waugh, R.C., Brown, R.S., Willoughby, P.G., 1990. Internal flow field studies in a simulated cylindrical port rocket chamber. *Journal of Propulsion and Power* 6, 690-704.
- Dunlap, R., Willoughby, P.G., Hermsen, R.W., 1974. Flowfield in the combustion chamber of a solid propellant rocket motor. *AIAA Journal* 12, 1440-1445.

- Flandro, G.A., 1974. Solid propellant acoustic admittance corrections. *Journal of Sound and Vibration* 36, 297-312.
- Griffond, J., Casalis, G., Pineau, J.-P., 2000. Spatial instability of flow in a semiinfinite cylinder with fluid injection through its porous walls. *European Journal of Mechanics B/Fluids* 19, 69-87.
- Larcombe, P., French, D., 2000. On the ‘Other’ Catalan Numbers: A Historical Formulation Re-examined. *Congr. Numer* 143, 33–64.
- Ma, Y., Van Moorhem, W.K., Shorthill, R.W., 1991. Experimental investigation of velocity coupling in combustion instability. *Journal of Propulsion and Power* 7, 692-699.
- Majdalani, J., 1995. Improved Flowfield Models in Rocket Motors and the Stokes Layer with Sidewall Injection. Department of Mechanical Engineering. University of Utah, Salt Lake City, UT.
- Majdalani, J., 1999a. The boundary layer structure in cylindrical rocket motors. *AIAA Journal* 37, 505-508.
- Majdalani, J., 1999b. Vortical and acoustical mode coupling inside a two-dimensional cavity with transpiring walls. *Journal of the Acoustical Society of America* 106, 46-56.
- Majdalani, J., 2001a. Improved solution for the vortical and acoustical mode coupling inside a two-dimensional cavity with porous walls. *Journal of the Acoustical Society of America* 109, 475-479.

- Majdalani, J., 2001b. The oscillatory channel flow with arbitrary wall injection. *Z. angew. Math. Phys. (ZAMP)* 52, 33-61.
- Majdalani, J., 2001c. Vorticity dynamics in isobarically closed porous channels. Part I: standard perturbations. *Journal of Propulsion and Power* 17, 355-362.
- Majdalani, J., 2009. Multiple asymptotic solutions for axially travelling waves in porous channels. *Journal of Fluid Mechanics* in press, 1-40.
- Majdalani, J., Flandro, G.A., 2002. The oscillatory pipe flow with arbitrary wall injection. *Proc. R. Soc. Lond.* 458, 1621-1651.
- Majdalani, J., Rienstra, S.W., 2002. Two asymptotic forms of the rotational solution for wave propagation inside viscous channels with transpiring walls. *Quarterly Journal of Mechanics and Applied Mathematics* 55, 141-162.
- Majdalani, J., Roh, T.S., 2000. The oscillatory channel flow with large wall injection. *Proceedings of the Royal Society, London* 456, 1625-1657.
- Majdalani, J., Roh, T.S., 2001. Vorticity dynamics in isobarically closed porous channels. Part II: space-reductive perturbations. *Journal of Propulsion and Power* 17, 363-370.
- Majdalani, J., Van Moorhem, W.K., 1997. A multiple-scales solution to the acoustic boundary layer in solid rocket motors. *J. Propulsion* 13, 186-193.
- Murdock, J., 1999. *Perturbations: theory and methods*, Society for Industrial Mathematics.

Richardson, E.G., Tyler, E., 1929. The transverse velocity gradient near the mouths of pipes in which an alternating or continuous flow of air is established. Proceedings of the Royal Society, London 42, 1-15.

Skalak, F.M., Wang, C.-Y., 1978. On the nonunique solutions of laminar flow through a porous tube or channel. SIAM Journal on Applied Mathematics 34, 535-544.

Taylor, G.I., 1956. Fluid flow in regions bounded by porous surfaces. Proceedings of the Royal Society, London 234, 456-475.

Terrill, R.M., 1983. Laminar flow in a porous tube. ASME Journal of Fluids Engineering 105, 303-307.

Terrill, R.M., Thomas, P.W., 1969. On laminar flow through a uniformly porous pipe. Applied Scientific Research 21, 37-67.

Weissberg, H.L., 1959. Laminar flow in the entrance region of a porous pipe. Physics of Fluids 2, 510-516.

Yuan, S.W., Finkelstein, A.B., 1956. Laminar pipe flow with injection and suction through a porous wall. Transactions of the American Society of Mechanical Engineers: Journal of Applied Mechanics 78, 719-724.

Vita

Nadim Zgheib was born in Hrajel, Lebanon on April 27, 1983. He attended Notre Dame University, where he received a Bachelor of Engineering degree in Mechanical Engineering in Spring 2007. While completing his undergraduate studies, Nadim competed as a professional basketball player at both the national and international levels. These activities enabled him to gain valuable team-building experience while helping him to develop appreciation for diverse cultures. Nadim studied Fluid Mechanics under the direction of Dr. Majdalani and will be graduating with a Master of Science degree in Aerospace Engineering in December 2009. He plans to continue his studies at the University of Tennessee Space Institute in pursuit of his doctoral degree.